

Self-organized photonic time quasicrystal from a single imposed clock

Minwook Kyung,^{1,*} Kyungmin Lee,^{1,*} Yung Kim,¹ Eun-Gook Moon,¹ Joonhee Choi,² and Bumki Min^{1,†}

¹*Department of Physics, Korea Advanced Institute of Science and Technology, Daejeon 34141, Republic of Korea*

²*Department of Electrical Engineering, Stanford University, Stanford, CA 94305, USA*

(Dated: May 8, 2026)

A photonic time crystal usually writes a clock into a medium. Here one clock does more than program the medium: it seeds a quasiperiodic temporal order that the nonlinear medium selects for itself. In a guided-wave lattice of nonlinear dipoles, a single-tone pump modulates the polarization sector, while Maxwell–polarization back-action selects two response frequencies whose only resolved low-order relation is the pump-locked sum condition. Their sum phase locks to the pump and the complementary phase winds, producing a photonic discrete time quasicrystal with torus-like phase dynamics and a discrete combination spectrum. Site-resolved measurements show locked-phase coherence across the measured lattice sites over a finite control-parameter window. These results establish a route from externally programmed time-varying media to self-organized temporal order in nonlinear photonic systems.

A photonic time crystal writes a clock into a medium. In nearly all realizations, that clock is imposed from outside: a time-periodic constitutive response couples Floquet harmonics separated by the modulation frequency, hybridizing frequencies while preserving momentum in spatially uniform media. This Maxwell–Floquet coupling opens momentum gaps [1–5]; it also enables parametric amplification, frequency conversion, and modified emission and absorption pathways [6–13]. Yet this success has defined a boundary: the temporal structure is prescribed and remains effectively independent of the electromagnetic state that evolves within it [2, 14, 15]. Microwave, metasurface, and parametric implementations likewise realize programmed temporal media rather than field-selected temporal order [16, 17]. The medium is therefore programmed to oscillate, but it does not choose its own temporal order. Once the driven polarization coordinate back-acts on the electromagnetic field, this separation between clock and response is no longer closed. In a nonlinear Maxwell–polarization medium, the imposed clock fixes only the external discrete time-translation symmetry; the long-time state can select additional phases that are not specified by the modulation waveform.

Time crystals distinguish a response that is merely driven from one that is dynamically selected. In periodically driven many-body systems, discrete time-translation symmetry can be broken so that long-time observables recur with period qT , rather than with the drive period T , with integer $q > 1$ [18–23]. This principle has been observed in quantum platforms [24–26], with related dissipative subharmonic order explored in optical resonators [27]. Its defining signature is rigidity, not frequency division alone: the response persists over a finite parameter range against perturbations that preserve the drive periodicity [28–30]. Photonics also offers a continuous-time counterpart, in which time-independent

coherent illumination drives plasmonic metamaterials into persistent, spatially ordered oscillations, including continuous space–time crystal states driven by nonreciprocal optical forces [31, 32]. Together, these developments establish self-organized temporal order as a robust nonequilibrium phenomenon. The Floquet–photonic challenge is sharper: can one imposed modulation period generate an additional temporal phase degree of freedom through the internal dynamics of a light–matter medium?

Quasiperiodicity is the stringent test of this self-selection mechanism. A second imposed tone would trivially provide a second frequency; here, no such tone is supplied. Instead, a medium driven by one clock must generate an additional internal phase degree of freedom. Experimentally, this appears as two response frequencies whose only resolved low-order relation with the drive is the pump-locked sum condition. The relevant finite-experiment distinction is therefore not a mathematical proof of irrationality from a finite record, but the exclusion of low-order rational closure that would reduce the response to a long-period limit cycle. Spatial quasicrystals established that long-range order need not rely on a primitive lattice period [33, 34], and recent work has extended this principle to time-quasicrystalline phases [35–41]. In a Floquet photonic medium, the corresponding state is neither a conventional subharmonic limit cycle nor a waveform programmed by quasiperiodic forcing. It is a two-frequency temporal order in which a pump-locked sum phase remains rigid while a complementary phase winds, producing an invariant circle in the stroboscopic section, or equivalently a torus in the dynamical description, rather than a closed finite-period orbit.

Here we demonstrate this photonic counterpart in a microwave guided-wave lattice of varactor-loaded nonlinear LC resonators. The microwave implementation is not a lumped-oscillator analogue of a photonic effect, but a field-resolved Maxwell–polarization medium: the varactor-loaded resonators provide pumped nonlinear polarization coordinates, while the guided electromagnetic mode hybridizes with them and mediates coupling across the array. This field-resolved access lets us resolve the in-

* These authors contributed equally to this work.

† bmin@kaist.ac.kr

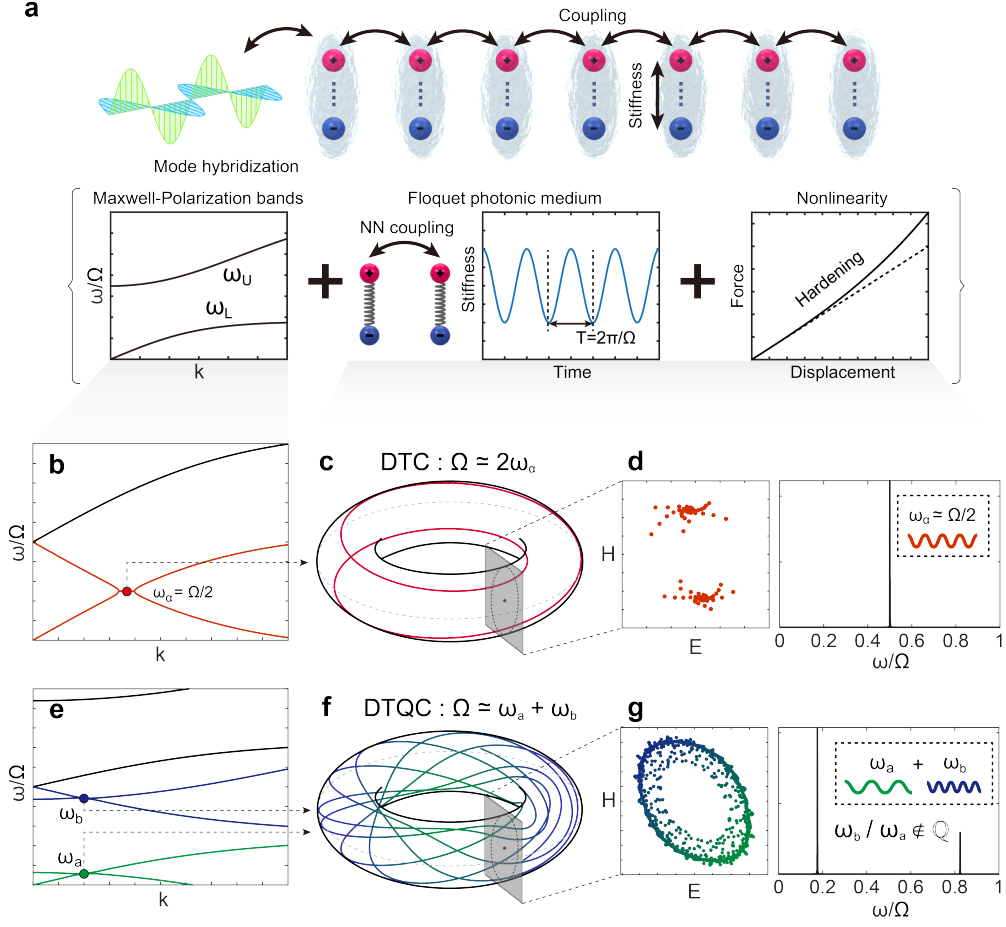


FIG. 1. Single-clock mechanism for self-organized temporal order in a Maxwell–polarization lattice. (a) A guided electromagnetic mode hybridizes with a Lorentz-type nonlinear polarization resonance. Nearest-neighbour polarization coupling, periodic stiffness modulation at angular frequency Ω , and onsite Duffing nonlinearity define a driven lattice whose long-time dynamics can stabilize either subharmonic or quasiperiodic temporal order. (b–d) DTC sector. A selected carrier from one hybrid band satisfies the degenerate parametric resonance condition $\Omega \simeq 2\omega_c$, yielding a period-doubled limit cycle, a two-point section, and a dominant subharmonic spectral peak. (e–g) DTQC sector. Two selected carriers, drawn from the lower and upper hybrid bands, satisfy the nondegenerate sum-resonance condition $\Omega \simeq \omega_a + \omega_b$. The pump locks their slow sum phase while the complementary phase winds, so the local attractor is an invariant torus rather than a limit cycle. The corresponding spectrum contains two self-selected fundamental response frequencies under a single imposed modulation.

gradient usually hidden in optical time-varying media—the self-consistent back-action between the electromagnetic field and the driven polarization sector. We identify the resulting spatially correlated two-frequency response as a photonic discrete time quasicrystal (DTQC): a quasiperiodic Floquet state selected by the medium rather than programmed into the drive.

We use the term photonic DTQC operationally. The drive contains a single imposed period $T = 2\pi/\Omega$; the steady state contains two internally selected spectral fundamentals; their sum phase remains locked to the pump; the complementary phase winds rather than locking to a finite-period orbit; and the locked phase is coherent across the measured lattice sites over a finite parameter window. In a finite experiment, quasiperiodicity is established by ruling out low-order rational closure within the

spectral resolution and observation time. The time dependence enters through the polarization sector, rather than through a prescribed $\varepsilon(t)$ inserted into Maxwell’s equations, revealing a route from one imposed clock to self-organized quasiperiodic temporal order through nonlinear Maxwell–polarization back-action.

To make the mechanism explicit, we start from a continuum Maxwell–Lorentz description of a guided-wave medium with a resonant nonlinear polarization coordinate $P(z, t)$. The electromagnetic field is closed by

$$\partial_z E = -\mu \partial_t H, \quad \partial_z H = -\partial_t (\varepsilon_b E + P), \quad (1)$$

and the polarization sector obeys

$$\ddot{P} + \gamma \dot{P} + \Omega_0^2(t)P + \beta P^3 - v_P^2 \partial_z^2 P = \chi E. \quad (2)$$

Here γ is the polarization damping rate, β the local Duff-

ing nonlinearity, v_P the polarization-coupling velocity, and χ the field–polarization coupling. The pump modulates the polarization stiffness,

$$\Omega_0^2(t) = \omega_0^2[1 + \delta \cos(\Omega t)], \quad (3)$$

so the imposed periodicity enters through an internal material degree of freedom rather than through a prescribed $\varepsilon(t)$ inserted directly into Maxwell’s equations. Here δ denotes the effective stiffness-modulation depth of the Maxwell–polarization model; its relation to the circuit-level resonator-capacitance modulation is given in Supplementary Section S2.

Equations (1) and (2) are the Maxwell–Lorentz form of a resonant dispersive photonic medium with a pumped nonlinear polarization coordinate. In optical and polaritonic platforms, P may represent an electronic, excitonic, phononic or polaritonic polarization coordinate, while $\Omega_0(t)$ or the corresponding oscillator strength can be tuned by optical or electrical pumping [4, 13, 42]. The cubic term is a Duffing nonlinearity of this polarization oscillator; after projection onto the hybrid Maxwell–polarization branches it produces Kerr-like self- and cross-nonlinearities, but the underlying response is resonant and dynamical rather than an instantaneous Kerr constitutive law. In the experimental microwave resonator array, $n = 1, \dots, N$ labels the unit cell, and the continuum coupling term is implemented by nearest-neighbour polarization coupling, $-v_P^2 \partial_z^2 P \rightarrow g(2P_n - P_{n+1} - P_{n-1})$, with $g \simeq v_P^2/d^2$ for unit-cell spacing d . Thus the array should be viewed as a discrete realization of the continuum Maxwell–polarization medium, rather than as a separate lumped-oscillator model; the explicit Langevin convention used to model injected noise is specified in Supplementary Section S1.

Experimentally, this medium is implemented as a one-dimensional guided-wave array of $N = 12$ varactor-loaded split-ring LC resonators (Supplementary Section S4 and Supplementary Fig. S4.1). A dc bias sets the varactor operating point, and a common single-tone radio-frequency pump modulates the resonator capacitance, thereby modulating the effective polarization stiffness. The DTC and DTQC sectors are accessed at modulation frequencies $f_{\text{mod}} = 2.98$ GHz and 2.47 GHz, respectively. Site-resolved voltages are recorded from selected unit cells, while calibrated broadband noise is injected from one end of the waveguide to tune S_{noise} . This microwave implementation therefore provides direct access to the field and polarization dynamics that are usually hidden in optical time-varying media.

Figure 1(a) summarizes the physical ingredients of the platform: a Lorentz-type polarization resonance hybridized with a guided electromagnetic mode, nearest-neighbour polarization coupling, periodic modulation of the polarization stiffness, and local Duffing nonlinearity. In the unmodulated linear limit, the Maxwell–Lorentz problem supports two polariton-like hybrid bands, denoted by the lower and upper branches $\omega_L(k)$ and $\omega_U(k)$ (Supplementary Section S1). Periodic stiffness modula-

tion then selects near-resonant carrier frequencies from these bands. In a degenerate channel, a selected carrier satisfies $\Omega \simeq 2\omega_\alpha$, producing a local period-doubled response (Fig. 1(b–d)). In a nondegenerate channel, two selected carriers, $\omega_a \simeq \omega_L(k_0)$ and $\omega_b \simeq \omega_U(k_0)$, with k_0 denoting the resonant momentum window, satisfy the sum-resonance condition $\Omega \simeq \omega_a + \omega_b$, so that the pump couples their slow sum phase (Fig. 1(e–g)). The former gives the local DTC channel; the latter gives the local DTQC channel. Electromagnetic coupling along the array then promotes these local phase-locking mechanisms into spatially correlated temporal order.

A branch-resolved normal form makes the two locking channels explicit. We project the driven Maxwell–polarization dynamics onto the selected near-resonant carrier sectors and retain the slow action–angle variables $J_{\alpha,n}$ and $\tilde{\theta}_{\alpha,n}$, where $\alpha = a, b$ labels the selected carrier sector and n labels the unit cell. The coefficients below are effective slow-Hamiltonian parameters obtained after hybrid-branch projection and rotating-wave averaging (Supplementary Section S2). Damping, noise, and nonlinear saturation are included separately in the driven-dissipative slow-flow dynamics; their role is to convert the resonant manifolds of the Hamiltonian normal form into attracting states. The stroboscopically averaged Hamiltonian is

$$\begin{aligned} \bar{\mathcal{H}} = \sum_n \left[\sum_{\alpha=a,b} \left\{ \Delta_\alpha J_{\alpha,n} + \frac{\Lambda_{\alpha\alpha}}{2} J_{\alpha,n}^2 + \frac{h_\alpha}{2} J_{\alpha,n} \cos(2\tilde{\theta}_{\alpha,n}) \right. \right. \\ \left. \left. - K_\alpha \sqrt{J_{\alpha,n} J_{\alpha,n+1}} \cos(\tilde{\theta}_{\alpha,n} - \tilde{\theta}_{\alpha,n+1}) \right\} + \Lambda_{ab} J_{a,n} J_{b,n} \right. \\ \left. - g_{ab} \sqrt{J_{a,n} J_{b,n}} \cos(\tilde{\theta}_{a,n} + \tilde{\theta}_{b,n}) \right]. \end{aligned} \quad (4)$$

Here Δ_α are rotating-frame detunings, $\Lambda_{\alpha\alpha}$ and Λ_{ab} are the Kerr-like self- and cross-nonlinearities generated by the Duffing polarization response, and K_α sets the spatial phase stiffness along the array. The h_α terms are intrabranch 2:1 locking terms: they pin $2\tilde{\theta}_{\alpha,n}$ and generate the two symmetry-related subharmonic sectors of a DTC. By contrast, in the nondegenerate DTQC branch, the intrabranch 2:1 terms are off resonant and are omitted from the branch-reduced Hamiltonian; the retained interbranch pump channel g_{ab} pins only the slow sum phase $\Theta_{+,n} = \tilde{\theta}_{a,n} + \tilde{\theta}_{b,n}$, while leaving the complementary phase free to wind. In the full driven-dissipative Maxwell–polarization dynamics, damping and nonlinear saturation convert these locking manifolds into the attracting limit cycle and attracting invariant torus shown in Fig. 1. Direct time-domain integrations of the corresponding full time-domain model confirm the same normal-form picture: the degenerate channel gives a two-point stroboscopic section, whereas the nondegenerate channel gives an extended stroboscopic manifold with bounded sum phase $\Theta_+ \equiv \tilde{\theta}_a + \tilde{\theta}_b$ and continuously winding complementary phase $\Theta_- \equiv \tilde{\theta}_a - \tilde{\theta}_b$ (Supplementary

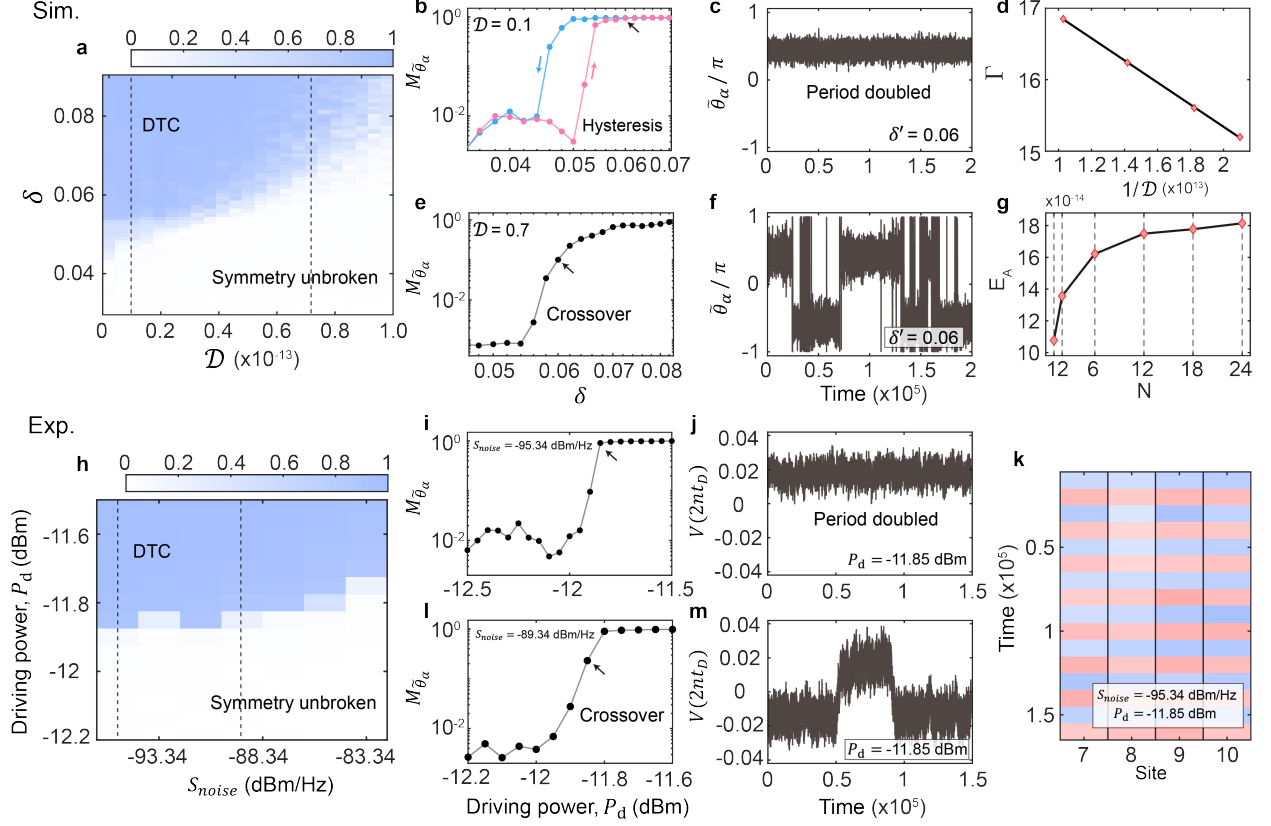


FIG. 2. Collective DTC order in the degenerate reference sector. (a–g) Simulation. (a) Numerical phase diagram in the (\mathcal{D}, δ) plane, showing a finite DTC window. (b,c) At moderate noise, $\mathcal{D} = 0.1$, the DTC order parameter exhibits hysteresis as δ is swept, and the rotating-frame phase $\bar{\theta}_\alpha/\pi$ remains bounded within the ordered regime. (d) The switching rate Γ shows approximately inverse dependence on $1/\mathcal{D}$. (e,f) At higher noise, $\mathcal{D} = 0.7$, the onset broadens into a crossover and the phase trace shows frequent stochastic switching. (g) Effective activation barrier E_A as a function of the number of coupled unit cells N . (h–m) Experiment. (h) Measured phase diagram in the (S_{noise}, P_d) plane, showing a finite DTC window. (i–k) At low injected noise, $S_{\text{noise}} = -95.34$ dBm/Hz, the DTC response shows an abrupt onset, stable period-doubled oscillations, and phase alignment across the measured sites. (l,m) At higher injected noise, $S_{\text{noise}} = -89.34$ dBm/Hz, the onset broadens into a smooth crossover.

Section S3). Equation (4) therefore places the DTC and DTQC mechanisms on the same Maxwell–polarization footing.

Equation (4) is therefore not a phenomenological fitting ansatz, but the lowest-order normal form allowed by the single-clock Floquet symmetry after projection onto the selected Maxwell–polarization branches. In the rotating-wave description, a phase term survives the period average only when it is neutral modulo the drive frequency Ω . The degenerate resonance $\Omega \simeq 2\omega_\alpha$ yields the intrabranch locking terms proportional to h_α , whereas the nondegenerate sum resonance $\Omega \simeq \omega_a + \omega_b$ yields the interbranch term proportional to g_{ab} . A single imposed clock can pin the sum phase, but it supplies no independent low-order term that pins the complementary phase. The sum-resonant channel therefore naturally supports a torus-like response at lowest order, unless an additional commensurability, symmetry constraint, or branch sup-

pression collapses it into a limit cycle.

At the level of a frozen-action phase reduction, the same normal form gives a useful leading-order estimate for the deterministic sum-locking tongue (Supplementary Section S3). We consider a spatially coherent DTQC state with finite saturated branch actions $\bar{J}_a, \bar{J}_b > 0$, neglect off-resonant intrabranch 2:1 locking terms in the nondegenerate sum-resonant sector, and absorb uniform spatial-stiffness shifts into the rotating-frame detunings. The nonlinear-shifted branch-sum detuning is then

$$\Delta_+^{\text{eff}} = \Delta_a + \Delta_b + \Lambda_{aa}\bar{J}_a + \Lambda_{bb}\bar{J}_b + \Lambda_{ab}(\bar{J}_a + \bar{J}_b). \quad (5)$$

The sum phase then obeys an Adler-type equation,

$$\begin{aligned} \dot{\Theta}_+ &= \Delta_+^{\text{eff}} - W_+ \cos(\Theta_+ - \Theta_0) + \dots, \\ W_+ &= \frac{|g_{ab}|}{2} \left(\sqrt{\frac{\bar{J}_b}{\bar{J}_a}} + \sqrt{\frac{\bar{J}_a}{\bar{J}_b}} \right), \end{aligned} \quad (6)$$

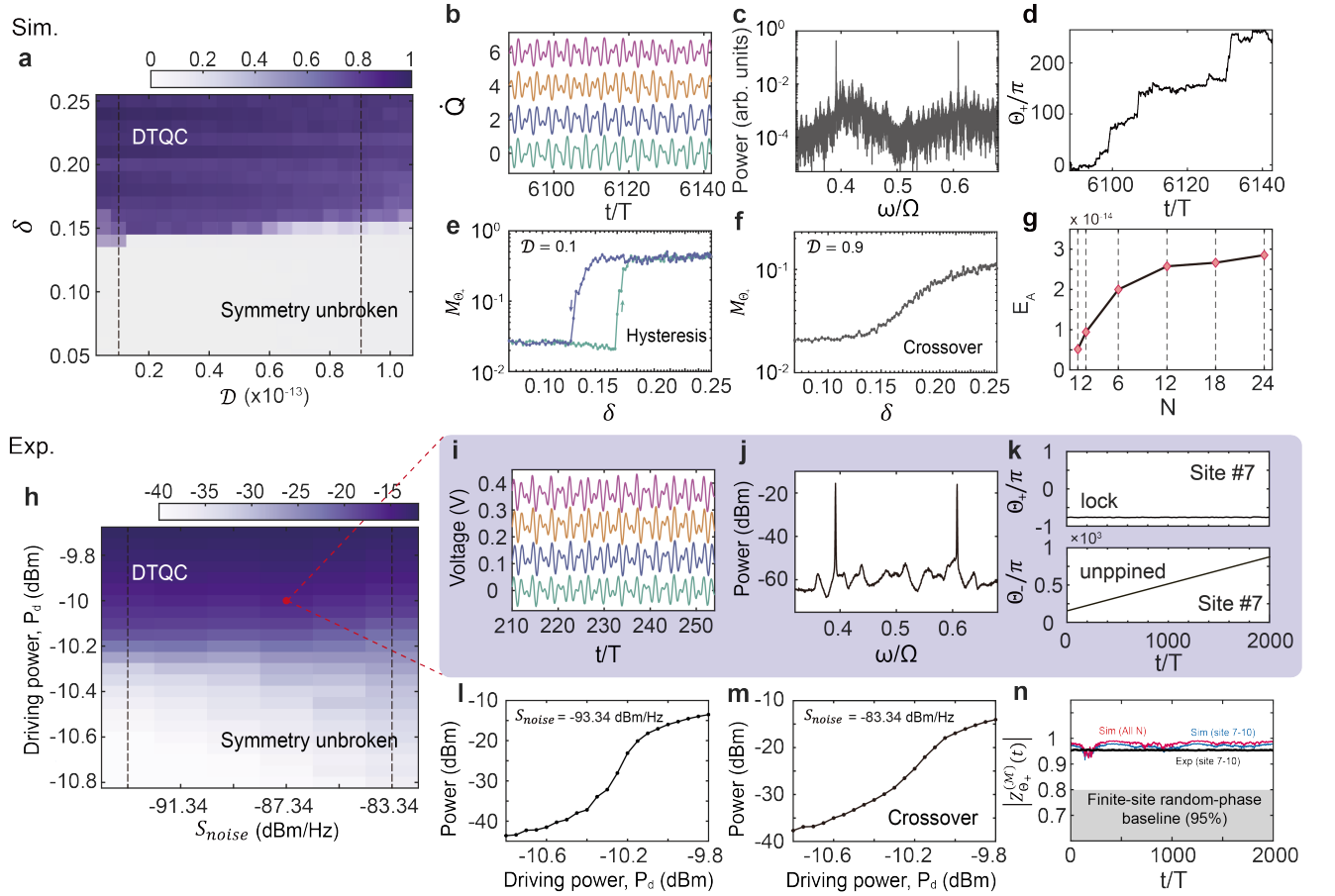


FIG. 3. Collective DTQC order from a single imposed modulation in the nondegenerate sum-resonant sector. (a) Numerical phase diagram in the (D, δ) plane, reconstructed from the sum-phase memory order parameter M_{Θ_+} , showing a finite DTQC window. (b,c) In the DTQC regime, the coupled array exhibits unit-cell-resolved quasiperiodic motion and a discrete steady-state spectrum with two clearly resolved peaks at ω_1 and ω_2 . (d) The sum phase remains locked for extended intervals, interrupted by occasional noise-induced slips. (e,f) At low noise ($D = 0.1$), the DTQC indicator shows hysteresis consistent with a first-order-like transition, whereas at higher noise ($D = 0.9$) it evolves through a smooth crossover. (g) The effective activation barrier E_A , extracted from rare Θ_+ -slip statistics in the noisy simulations, increases with the number of coupled unit cells N , indicating collective stabilization of the ordered quasiperiodic state. (h) Experimental phase diagram in the (S_{noise}, P_d) plane, reconstructed from the spectral proxy $M_{\text{DTQC}}^{\text{spec}}$, showing a finite DTQC window. (i,j) Measured voltages and steady-state spectrum at the marked operating point in (h) support a spatially correlated quasiperiodic response across the measured sites and show two clearly resolved peaks at ω_1 and ω_2 . (k) Experimental phase reconstruction at the representative operating point, showing the locked sum phase and the unpinned complementary phase. (l,m) Noise-dependent experimental DTQC line cuts: at lower injected noise, $S_{\text{noise}} = -93.34$ dBm/Hz, the DTQC indicator exhibits a sharper onset, whereas at higher injected noise, $S_{\text{noise}} = -83.34$ dBm/Hz, it evolves through a smooth crossover. (n) The measured-site coherence $|Z_{\Theta_+}^{(M)}(t)|$ remains above the 95% finite-site random-phase baseline and agrees with the simulations.

where Θ_0 absorbs the phase convention of the pump coupling, and W_+ denotes the reduced sum-phase locking bandwidth. Thus, within this frozen-action phase reduction, a deterministic sum-locked solution requires

$$|\Delta_+^{\text{eff}}| \leq W_+. \quad (7)$$

This estimate captures the leading-order sum-locking tongue of the normal form. The observed DTQC window further requires stable nonlinear saturation of both branch actions, transverse stability of the torus, suppression of low-order complementary-phase locking, and

sufficient robustness against noise-induced slips and dephasing. These requirements are tested below through the finite DTQC window, activation-barrier scaling, measured-site coherence, and low-order quasiperiodicity diagnostics.

We first use the degenerate 2:1 channel as a periodic reference sector. Its role is to calibrate collective subharmonic locking in the same Maxwell–polarization lattice before we test the more stringent sum-resonant DTQC channel. Figure 2 shows that this channel forms a collective DTC response in both simulation and experiment. In

simulations, we characterize the ordered phase through the site-set-averaged complex phase memory

$$Z_{\varphi}^{(\mathcal{S})}(t) \equiv \frac{1}{N_{\mathcal{S}}} \sum_{n \in \mathcal{S}} e^{i\Delta\varphi_n(t)}, \quad (8)$$

where $\Delta\varphi_n(t) \equiv \varphi_n(t) - \varphi_n(t_{\text{ref}})$. Here t_{ref} is the first time point of the post-transient analysis window, \mathcal{S} denotes the site set used in the corresponding analysis, and $N_{\mathcal{S}} = |\mathcal{S}|$. In the DTC sector, $\varphi_n = \tilde{\theta}_{\alpha,n}$, where $\tilde{\theta}_{\alpha,n}$ is the rotating-frame phase of the resonant hybrid branch. The corresponding late-time phase-memory order parameter is $M_{\tilde{\theta}_{\alpha}} = \left| \langle Z_{\tilde{\theta}_{\alpha}}^{(\mathcal{S})}(t) \rangle_t \right|$. This quantity identifies a finite ordered window in the (\mathcal{D}, δ) plane (Fig. 2(a)). Within this window the rotating-frame phase remains bounded and the response is $2T$ -periodic; outside it, phase slips and dephasing suppress the phase memory. Low-noise line cuts show a hysteretic onset with rare activated switching, whereas stronger noise broadens the onset into a crossover (Fig. 2(b–f)). The effective activation barrier extracted from phase-slip statistics grows with the number of coupled cells before saturating, consistent with collective stabilization by short-range coupling (Fig. 2(g)) [43, 44]. The phase-slip counting procedure is described in Supplementary Section S3.

The experiment shows the same noise-controlled reference-sector phenomenology. As a function of drive power P_d and injected noise spectral density S_{noise} , the measured phase diagram reveals a finite DTC window (Fig. 2(h)). At lower injected noise, increasing P_d produces a threshold-like onset of stable $2T$ -periodic voltage oscillations together with phase alignment across the measured sites (Fig. 2(i–k)); at higher injected noise, the onset broadens into a smooth crossover (Fig. 2(l,m)). These results establish the degenerate channel as a collective, noise-robust subharmonic reference state. We now turn to the sum-resonant channel, where the same single imposed modulation supports a spatially correlated quasiperiodic response whose local attractor is an invariant torus rather than a limit cycle.

We do not identify the DTQC regime from a two-peak spectrum alone. Instead, we require a hierarchy of signatures that separates a self-selected quasiperiodic Floquet state from ordinary frequency conversion or weak long-period locking. First, the pump is single-tone, while the steady state contains two response fundamentals. Second, the sum phase is locked to the pump and the complementary phase winds. Third, the locked phase is coherent across the measured sites over a finite control-parameter window. Finally, low-order commensurability and recurrence diagnostics rule out collapse into a finite-period orbit within the experimental resolution.

Unlike the DTC reference, the sum-resonant response is not characterized by a single subharmonic period. Instead, the pump locks only the branch-sum phase, $\Theta_+ = \tilde{\theta}_a + \tilde{\theta}_b$, while the complementary phase, $\Theta_- = \tilde{\theta}_a - \tilde{\theta}_b$, continues to wind. The corresponding local attractor is therefore a two-frequency torus rather than a limit cy-

cle. Electromagnetic coupling promotes this torus into a spatially correlated quasiperiodic response. We identify this coupled, finite-window regime as the DTQC sector of the driven Maxwell–polarization lattice. To locate this regime numerically, we use the effective modulation depth δ and the dimensionless simulation noise intensity \mathcal{D} as control parameters. In the DTQC sector, the phase variable entering Eq. (8) is $\varphi_n = \Theta_{+,n}$, so that the corresponding sum-phase memory order parameter is

$$M_{\Theta_+} = \left| \langle Z_{\Theta_+}^{(\mathcal{S})}(t) \rangle_t \right|. \quad (9)$$

This quantity remains large when the sum phase stays locked over long times and is suppressed by Θ_+ -slips and dephasing outside the ordered regime. For direct comparison with experiment, we additionally evaluate the spectral proxy $M_{\text{DTQC}}^{\text{spec}} = (A_1^{\text{pk}} A_2^{\text{pk}})^{1/2}$, where $A_{1,2}^{\text{pk}}$ are the peak levels of the two dominant response components in the steady-state local spectrum (Supplementary Section S4). Because this quantity becomes large only when both fundamentals are simultaneously present, it provides an experimentally accessible indicator of the same DTQC window.

The resulting numerical phase diagram reveals a finite DTQC window in the (\mathcal{D}, δ) plane (Fig. 3(a)). Within this window, the unit-cell-resolved dynamics exhibits long-lived quasiperiodic motion (Fig. 3(b)), the steady-state spectrum contains two clearly separated peaks at the self-selected frequencies ω_1 and ω_2 (Fig. 3(c)), and the sum-phase trace remains locked over long intervals, interrupted only by occasional noise-induced slips (Fig. 3(d)). Under a single periodic pump, the system therefore selects a frequency split in the sum-resonant channel, rather than reproducing a quasiperiodic waveform programmed into the drive.

The DTQC window shows the same noise-controlled phenomenology as the DTC reference, but with a softer locking scale. At $\mathcal{D} = 0.1$, the DTQC indicator exhibits hysteresis as δ is swept (Fig. 3(e)), consistent with first-order-like switching on accessible timescales. At $\mathcal{D} = 0.9$, the corresponding line cut evolves smoothly into the quasiperiodic phase (Fig. 3(f)), indicating a noise-broadened crossover. Rare Θ_+ -slip statistics yield an effective activation barrier E_A , which grows with the number of coupled cells before saturating (Fig. 3(g)), consistent with collective stabilization by short-range coupling (Supplementary Section S3). Compared with the DTC reference sector (Fig. 2(g)), the DTQC barrier is smaller, consistent with the softer locking structure of a torus: the pump pins only the sum phase, while the complementary phase remains free to wind.

Experimentally, the DTQC is accessed through site-resolved voltages and their steady-state spectra. Reconstructing the phase diagram in the (S_{noise}, P_d) plane from the spectral proxy $M_{\text{DTQC}}^{\text{spec}}$ reveals a finite DTQC window (Fig. 3(h)). Within this window, the measured voltages remain correlated across the simultaneously recorded sites (Fig. 3(i)), and the corresponding spectrum exhibits

two clearly resolved peaks at ω_1 and ω_2 (Fig. 3(j)). Because the pump is single-tone, these two fundamentals are not externally supplied as separate tones; they are selected by the driven lattice in the sum-resonant channel. This is the central control built into the experiment: no second temporal lattice vector is supplied by the source, yet two phases are required to describe the steady state. Phase reconstruction using response-frequency-resolved analytic signals further shows a locked sum phase and complementary-phase winding at a representative operating point (Fig. 3(k)). Noise-dependent experimental line cuts support the same picture: at lower injected noise, $S_{\text{noise}} = -93.34$ dBm/Hz, the DTQC indicator shows a sharper onset as P_d is varied (Fig. 3(l)), whereas at higher injected noise, $S_{\text{noise}} = -83.34$ dBm/Hz, the onset broadens into a smooth crossover (Fig. 3(m)), consistent with the high-noise numerical regime. Details of the measured-site set and the representative-site reconstruction are given in Supplementary Section S4.

For the simultaneously recorded measured-site set \mathcal{M} , the corresponding time-resolved measured-site coherence of the locked sum phase is simply $|Z_{\Theta_+}^{(\mathcal{M})}(t)|$. Here \mathcal{M} is the simultaneously recorded site set and $N_{\mathcal{M}} = |\mathcal{M}|$. Both the measured and simulated coherences remain above the finite-site random-phase baseline (Fig. 3(n)), showing that the DTQC response is spatially correlated across the measured sites rather than confined to a single local two-frequency oscillator. Supplementary Section S4 provides pairwise, distance-resolved, and subset-robust analyses showing that the coherence is distributed across site pairs and is not dominated by one measured channel or by a particular subset choice.

Because an infinite-time irrational frequency ratio cannot be proven from a finite experimental trace, Fig. 4 uses the appropriate finite-resolution criterion: it tests whether any low-order rational relation, other than the imposed sum resonance, closes the orbit within the observation window (Supplementary Section S4). The low-order relation map in Fig. 4(a) asks whether the extracted frequencies ω_1 and ω_2 satisfy any additional small-integer relation with the drive beyond the expected sum-resonant condition. Within the experimental frequency resolution, the only near-commensurate structure is the trivial family generated by $\omega_1 + \omega_2 \simeq \Omega$, whereas other low-order candidates remain clearly detuned.

Consistently, the measured steady-state spectrum in Fig. 4(b) is organized by the same two extracted fundamentals and their combination lines. This construction does not introduce extra fitting frequencies: the displayed lines are generated from the same (ω_1, ω_2) pair used for phase reconstruction. In the half-pump rotating two-phase representation at the representative site $n_0 = 7$, the reconstructed trajectory winds on the phase torus $(\tilde{\phi}_{1,n_0}, \tilde{\phi}_{2,n_0})$, consistent with a locked sum phase and an unpinned complementary phase (Fig. 4(c)). The recurrence diagnostic in Fig. 4(d) shows finite-time near returns of this winding trajectory, while the low-order relation map in Fig. 4(a) excludes an additional

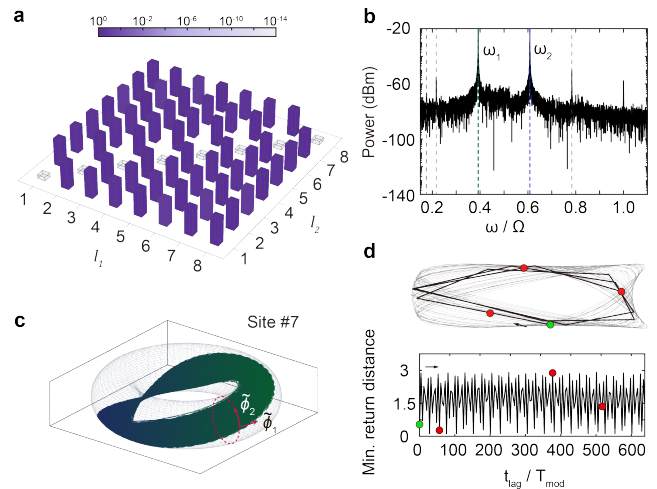


FIG. 4. Quasiperiodicity of the experimental DTQC state in spectrum, two-phase reconstruction, and recurrence. (a) Low-order relation map constructed from the extracted spectral pair (ω_1, ω_2) , showing the minimized mismatch $\min_{l_3 \in \mathbb{Z}} |l_1 \omega_1 + l_2 \omega_2 - l_3 \Omega| / \Omega$ over low-order integers (l_1, l_2) . The low-mismatch diagonal corresponds to trivial multiples of the expected sum-resonant condition $\omega_1 + \omega_2 \simeq \Omega$, while other low-order candidates remain strongly detuned. (b) Measured steady-state spectrum at the same operating point, overlaid with combination lines generated from the extracted fundamentals ω_1 and ω_2 . (c) Reconstructed two-phase trajectory at the representative site $n_0 = 7$, plotted on the half-pump rotating phase torus $(\tilde{\phi}_{1,n_0}, \tilde{\phi}_{2,n_0})$, showing a winding trajectory set by the locked sum phase and the unpinned complementary phase. (d) Recurrence diagnostic of the same reconstructed two-phase trajectory, showing finite-time near returns without evidence for an additional low-order closure beyond the pump-locked sum relation.

low-order closure beyond the pump-locked sum relation. Taken together with the locked-sum-phase reconstruction and measured-site coherence shown in Fig. 3, these diagnostics rule out the experimentally relevant alternatives—single-branch frequency conversion, low-order long-period locking, and an incoherent local oscillator response—and support the DTQC interpretation.

In our driven Maxwell–polarization lattice, temporal order is selected by nonlinear light–matter back-action. Near the nondegenerate sum resonance of two selected hybrid carriers, a single-tone pump generates two self-selected response frequencies: their sum phase is locked to the pump while the complementary phase winds. The resulting state is a spatially correlated photonic discrete time quasicrystal, supported by a two-frequency combination spectrum, torus-like two-phase dynamics, measured-site coherence and low-order commensurability diagnostics. The same platform also supports DTCs at the corresponding degenerate resonances, providing a periodic reference sector. Thus one Maxwell–polarization lattice realizes both a limit-cycle time crystal and a torus-like time quasicrystal, selected by different symmetry-allowed resonance channels of the same imposed clock.

More broadly, this work suggests a route to self-organized temporal photonic matter, in which the time structure of a medium is not fully prescribed by an external modulation but selected by nonlinear light–matter dynamics. The present microwave implementation provides field-resolved access to the Maxwell–polarization mechanism, while analogous ingredients—resonant polarization coordinates, tunable stiffness or oscillator strength, controlled loss and nonlinear saturation—appear in optical and polaritonic platforms such as epsilon-near-zero transparent conducting oxides, semiconductor metasurfaces and mid-infrared polaritonic Drude–Lorentz media [4, 13, 42]. Extending the DTQC state to such platforms will require many-cycle modulation with controlled dissipation and saturation, but the normal-form mechanism demonstrated here establishes

how a single imposed clock can lock one collective phase while leaving an internally selected complementary phase to wind, thereby producing quasiperiodic temporal order not encoded in the drive.

ACKNOWLEDGEMENTS

This work was supported by the National Research Foundation of Korea (NRF) through the government of Korea (NRF-2022R1A2C301335313) and the Samsung Science and Technology Foundation (SSTF-BA2402-02). J.C. acknowledges support from AFOSR (YIP No. FA9550-25-1-0147) and the Terman Faculty Fellowship at Stanford University.

-
- [1] J. Reyes-Ayona and P. Halevi, Observation of genuine wave vector (k or β) gap in a dynamic transmission line and temporal photonic crystals, *Applied Physics Letters* **107**, 074101 (2015).
- [2] J. S. Martínez-Romero, O. M. Becerra-Fuentes, and P. Halevi, Temporal photonic crystals with modulations of both permittivity and permeability, *Physical Review A* **93**, 063813 (2016).
- [3] M. M. Asgari, P. Garg, X. Wang, M. S. Mirmoosa, C. Rockstuhl, and V. Asadchy, Theory and applications of photonic time crystals: a tutorial, *Advances in Optics and Photonics* **16**, 958 (2024).
- [4] X. Wang, P. Garg, M. Mirmoosa, A. Lamprianidis, C. Rockstuhl, and V. Asadchy, Expanding momentum bandgaps in photonic time crystals through resonances, *Nature Photonics* **19**, 149 (2025).
- [5] N. Wang, Z.-Q. Zhang, and C. T. Chan, Photonic floquet media with a complex time-periodic permittivity, *Physical Review B* **98**, 085142 (2018).
- [6] E. Galiffi, R. Tirole, S. Yin, H. Li, S. Vezzoli, P. A. Huidobro, M. G. Silveirinha, R. Sapienza, A. Alù, and J. Pendry, Photonics of time-varying media, *Advanced Photonics* **4**, 014002 (2022).
- [7] J. Park, K. Lee, R.-Y. Zhang, H.-C. Park, J.-W. Ryu, G. Y. Cho, M. Y. Lee, Z. Zhang, N. Park, W. Jeon, et al., Spontaneous emission decay and excitation in photonic time crystals, *Physical Review Letters* **135**, 133801 (2025).
- [8] K. Lee, M. Kyung, Y. Kim, J. Park, H. Lee, J. Choi, C. Chan, J. Shin, K. W. Kim, and B. Min, Analogs of spontaneous emission and lasing in photonic time crystals, *Physical Review Letters* **136**, 093802 (2026).
- [9] J. E. Sustaeta-Osuna, F. J. García-Vidal, and P. Huidobro, Quantum theory of photon pair creation in photonic time crystals, *ACS Photonics* **12**, 1873 (2025).
- [10] J. Bae, K. Lee, B. Min, and K. W. Kim, Quantum electrodynamics of photonic time crystals, *Nature Communications* **17**, 858 (2026).
- [11] Z. Dong, X. Chen, and L. Yuan, Extremely narrow band in moiré photonic time crystal, *Physical Review Letters* **135**, 033803 (2025).
- [12] J. Feinberg, D. E. Fernandes, B. Shapiro, and M. G. Silveirinha, Plasmonic time crystals, *Physical Review Letters* **134**, 183801 (2025).
- [13] T. F. Allard, J. E. Sustaeta-Osuna, F. J. García-Vidal, and P. A. Huidobro, Broadband dipole absorption in dispersive photonic time crystals, *Physical Review Letters* **136**, 106903 (2026).
- [14] J. Park, H. Cho, S. Lee, K. Lee, K. Lee, H. C. Park, J.-W. Ryu, N. Park, S. Jeon, and B. Min, Revealing non-hermitian band structure of photonic floquet media, *Science Advances* **8**, eabo6220 (2022).
- [15] M. Lyubarov, Y. Lumer, A. Dikopoltsev, E. Lustig, Y. Sharabi, and M. Segev, Amplified emission and lasing in photonic time crystals, *Science* **377**, 425 (2022).
- [16] X. Wang, M. S. Mirmoosa, V. S. Asadchy, C. Rockstuhl, S. Fan, and S. A. Tretyakov, Metasurface-based realization of photonic time crystals, *Science Advances* **9**, eadg7541 (2023).
- [17] J. S. Martínez-Romero and P. Halevi, Parametric resonances in a temporal photonic crystal slab, *Physical Review A* **98**, 053852 (2018).
- [18] F. Wilczek, Quantum time crystals, *Physical Review Letters* **109**, 160401 (2012).
- [19] A. Shapere and F. Wilczek, Classical time crystals, *Physical Review Letters* **109**, 160402 (2012).
- [20] D. V. Else, B. Bauer, and C. Nayak, Floquet time crystals, *Physical Review Letters* **117**, 090402 (2016).
- [21] N. Y. Yao, A. C. Potter, I.-D. Potirniche, and A. Vishwanath, Discrete time crystals: Rigidity, criticality, and realizations, *Physical Review Letters* **118**, 030401 (2017).
- [22] D. V. Else, C. Monroe, C. Nayak, and N. Y. Yao, Discrete time crystals, *Annual Review of Condensed Matter Physics* **11**, 467 (2020).
- [23] S. Yi-Thomas and J. D. Sau, Theory for dissipative time crystals in coupled parametric oscillators, *Physical Review Letters* **133**, 266601 (2024).
- [24] S. Choi, J. Choi, R. Landig, G. Kucsko, H. Zhou, J. Isoya, F. Jelezko, S. Onoda, H. Sumiya, V. Khemani, et al., Observation of discrete time-crystalline order in a disordered dipolar many-body system, *Nature* **543**, 221 (2017).
- [25] J. Zhang, P. W. Hess, A. Kyprianidis, P. Becker, A. Lee, J. Smith, G. Pagano, I.-D. Potirniche, A. C. Potter,

- A. Vishwanath, *et al.*, Observation of a discrete time crystal, *Nature* **543**, 217 (2017).
- [26] A. Kyprianidis, F. Machado, W. Morong, P. Becker, K. S. Collins, D. V. Else, L. Feng, P. W. Hess, C. Nayak, G. Pagano, *et al.*, Observation of a prethermal discrete time crystal, *Science* **372**, 1192 (2021).
- [27] H. Taheri, A. B. Matsko, L. Maleki, and K. Sacha, All-optical dissipative discrete time crystals, *Nature Communications* **13**, 848 (2022).
- [28] N. Y. Yao, C. Nayak, L. Balents, and M. P. Zaletel, Classical discrete time crystals, *Nature Physics* **16**, 438 (2020).
- [29] T. L. Heugel, M. Oscity, A. Eichler, O. Zilberberg, and R. Chitra, Classical many-body time crystals, *Physical Review Letters* **123**, 124301 (2019).
- [30] M. P. Zaletel, M. Lukin, C. Monroe, C. Nayak, F. Wilczek, and N. Y. Yao, Colloquium: Quantum and classical discrete time crystals, *Reviews of Modern Physics* **95**, 031001 (2023).
- [31] T. Liu, J.-Y. Ou, K. F. MacDonald, and N. I. Zheludev, Photonic metamaterial analogue of a continuous time crystal, *Nature Physics* **19**, 986 (2023).
- [32] V. Raskatla, T. Liu, J. Li, K. F. MacDonald, and N. I. Zheludev, Continuous space-time crystal state driven by nonreciprocal optical forces, *Physical Review Letters* **133**, 136202 (2024).
- [33] D. Shechtman, I. Blech, D. Gratias, and J. W. Cahn, Metallic phase with long-range orientational order and no translational symmetry, *Physical Review Letters* **53**, 1951 (1984).
- [34] D. Levine and P. J. Steinhardt, Quasicrystals: A new class of ordered structures, *Physical Review Letters* **53**, 2477 (1984).
- [35] S. Autti, V. Eltsov, and G. Volovik, Observation of a time quasicrystal and its transition to a superfluid time crystal, *Physical Review Letters* **120**, 215301 (2018).
- [36] A. Pizzi, J. Knolle, and A. Nunnenkamp, Period- n discrete time crystals and quasicrystals with ultracold bosons, *Physical Review Letters* **123**, 150601 (2019).
- [37] H. Zhao, F. Mintert, and J. Knolle, Floquet time spirals and stable discrete-time quasicrystals in quasiperiodically driven quantum many-body systems, *Physical Review B* **100**, 134302 (2019).
- [38] D. V. Else, W. W. Ho, and P. T. Dumitrescu, Long-lived interacting phases of matter protected by multiple time-translation symmetries in quasiperiodically driven systems, *Physical Review X* **10**, 021032 (2020).
- [39] Z. G. Nicolaou and A. E. Motter, Anharmonic classical time crystals: A coreonance pattern formation mechanism, *Physical Review Research* **3**, 023106 (2021).
- [40] G. He, B. Ye, R. Gong, C. Yao, Z. Liu, K. W. Murch, N. Y. Yao, and C. Zu, Experimental realization of discrete time quasicrystals, *Physical Review X* **15**, 011055 (2025).
- [41] X. Feng, S. Liu, S. Chen, and S.-X. Zhang, Tunable discrete quasi-time crystal from a single drive (2025), arXiv:2512.10303, arXiv:2512.10303 [quant-ph].
- [42] M. R. Shcherbakov, K. Werner, Z. Fan, N. Talisa, E. Chowdhury, and G. Shvets, Photon acceleration and tunable broadband harmonics generation in nonlinear time-dependent metasurfaces, *Nature Communications* **10**, 1345 (2019).
- [43] R. S. Maier and D. L. Stein, Noise-activated escape from a sloshing potential well, *Physical Review Letters* **86**, 3942 (2001).
- [44] H. B. Chan and C. Stambaugh, Activation barrier scaling and crossover for noise-induced switching in micromechanical parametric oscillators, *Physical Review Letters* **99**, 060601 (2007).

Supplementary Information: Self-organized photonic time quasicrystal from a single imposed clock

Minwook Kyung^{1,*}, Kyungmin Lee^{1,*}, Yung Kim¹, Eun-Gook Moon¹, Joonhee Choi² and Bumki Min^{1,†}

¹*Department of Physics, Korea Advanced Institute of Science and Technology, Daejeon 34141, Republic of Korea*

²*Department of Electrical Engineering, Stanford University, Stanford, CA 94305, USA*

**These authors contributed equally to this work.*

[†] *bmin@kaist.ac.kr*

- **Section S1. Maxwell–Lorentz equations of motion and hybrid carrier basis**

- Maxwell–polarization equations
- First-order state-space form
- Unmodulated hybrid carriers
- Resonance conditions and selected carrier sectors

- **Section S2. Circuit realization and projected slow Hamiltonian**

- Flux–charge circuit model
- Reduced capacitive Hamiltonian
- Weak modulation and reduced circuit Hamiltonian
- Two-sector slow variables
- Hybrid basis and unified slow Hamiltonian

- **Section S3. Branch decomposition: degenerate DTC channels and nondegenerate DTQC channel**

- Linear Floquet branch landscape
- Branch I-A: DTC_a from $\Omega \simeq 2\omega_a$
- Branch I-B: DTC_b from $\Omega \simeq 2\omega_b$
- Branch II: DTQC from $\Omega \simeq \omega_a + \omega_b$
- Frozen-action phase reduction and deterministic sum-locking tongue
- Slow-flow equations and noise projection
- Validation against the full time-domain model

- **Section S4. Experimental implementation**

- Experimental platform, measurement setup, and noise injection
- Signal processing and reconstruction of experimental DTQC observables
- Quantitative quasiperiodicity diagnostics for the experimental DTQC state
- Pairwise, distance-resolved, and subset-robust spatial coherence of the experimental DTQC state

S1. MAXWELL–LORENTZ EQUATIONS OF MOTION AND HYBRID CARRIER BASIS

A. Maxwell–polarization equations

We consider a one-dimensional Maxwell–Lorentz medium with a nonlinear polarization coordinate $P(z, t)$. We introduce a guided-wave coordinate $\Phi(z, t)$ such that the local electric field is the generalized velocity

$$E(z, t) \equiv \dot{\Phi}(z, t). \quad (\text{S1})$$

The displacement field is

$$D(z, t) = \varepsilon_b E(z, t) + P(z, t), \quad (\text{S2})$$

and the corresponding displacement-like canonical momentum density is

$$Q(z, t) \equiv D(z, t) = \varepsilon_b \dot{\Phi}(z, t) + P(z, t), \quad E(z, t) = \frac{Q(z, t) - P(z, t)}{\varepsilon_b}. \quad (\text{S3})$$

For a source-free one-dimensional guided mode with transverse fields, Maxwell's equations reduce to

$$\partial_z E(z, t) = -\mu \partial_t H(z, t), \quad \partial_z H(z, t) = -\partial_t D(z, t) = -\partial_t Q(z, t). \quad (\text{S4})$$

Using $E = \dot{\Phi}$ in the first equation gives $\partial_t(\partial_z \Phi + \mu H) = 0$. For the oscillatory fields considered here, we set the time-independent integration constant to zero and obtain

$$H(z, t) = -\frac{1}{\mu} \partial_z \Phi(z, t). \quad (\text{S5})$$

Substitution into the second Maxwell equation gives

$$\dot{Q}(z, t) = \frac{1}{\mu} \partial_z^2 \Phi(z, t). \quad (\text{S6})$$

Equations (S3) and (S6) provide the first-order guided-wave sector, with the physical fields recovered through

$$E = \frac{Q - P}{\varepsilon_b}, \quad H = -\frac{1}{\mu} \partial_z \Phi. \quad (\text{S7})$$

The polarization is modeled as a nonlinear Lorentz oscillator driven by the local electric field,

$$\ddot{P} + \gamma \dot{P} + \Omega_0^2(t)P + \beta P^3 - v_P^2 \partial_z^2 P = \chi E + \frac{1}{m} F(z, t). \quad (\text{S8})$$

Here γ is the polarization damping rate, β is the Duffing nonlinearity, v_P is the polarization-coupling velocity, χ is the field–polarization coupling, and F is an effective Langevin force. The parameter m fixes the canonical normalization of the polarization momentum and the corresponding normalization of the Langevin force term. Since P is normalized as the polarization entering $D = \varepsilon_b E + P$, we use the convention $\Pi \equiv m\dot{P}$ and $m\chi = 1$. This is a normalization convention for the chosen polarization coordinate, not an additional physical constraint.

The imposed periodic drive modulates the polarization stiffness,

$$\Omega_0^2(t) = \omega_0^2 [1 + \delta \cos(\Omega t)], \quad T = \frac{2\pi}{\Omega}. \quad (\text{S9})$$

Thus the explicit time dependence enters through an internal material coordinate rather than through a prescribed instantaneous $\varepsilon(t)$.

For the discrete dipole lattice used to connect with the experimental array, $z_n = nd$ and $P_n(t) \equiv P(z_n, t)$. With the standard central-difference convention,

$$-v_P^2 \partial_z^2 P(z_n, t) \longrightarrow g(2P_n - P_{n+1} - P_{n-1}), \quad g = \frac{v_P^2}{d^2}.$$

Accordingly, Eq. (S8) becomes

$$\ddot{P}_n + \gamma \dot{P}_n + \Omega_0^2(t)P_n + \beta P_n^3 + g(2P_n - P_{n+1} - P_{n-1}) = \chi E_n + \frac{1}{m} F_n(t), \quad (\text{S10})$$

where $E_n(t)$ is the guided electromagnetic field evaluated at the n -th unit cell, not an externally prescribed waveform. The discrete equation is therefore a lattice realization of the same Maxwell–polarization medium, rather than a separate lumped-oscillator model.

For stochastic time-domain simulations, we use the lattice-level Langevin convention directly. The continuum Maxwell–polarization equations above serve as the deterministic parent model, while the noise used to construct the numerical phase diagrams is applied to the discrete polarization coordinates. In dimensional variables we write

$$\langle F_n(t) \rangle = 0, \quad \langle F_n(t) F_m(t') \rangle = 2m\gamma D_{\text{phys}} \delta_{nm} \delta(t - t'). \quad (\text{S11})$$

Here D_{phys} is an effective dimensional noise scale conjugate to the polarization coordinate. It should not be identified directly with the measured microwave noise spectral density S_{noise} , because the latter is the externally injected broadband noise before projection through the waveguide, coupling network, and resonator response.

For the numerical phase diagrams we use dimensionless variables

$$\tau = \omega_* t, \quad p_n = P_n / P_*.$$

In the Maxwell–Lorentz normalization used here, we choose

$$\omega_* = \omega_0, \quad P_* = \frac{\omega_0}{\sqrt{|\beta|}},$$

so that the Duffing coefficient in the dimensionless polarization equation is reduced to its sign. Defining

$$f_n(\tau) = \frac{F_n(t)}{mP_*\omega_*^2},$$

Eq. (S11) becomes

$$\langle f_n(\tau) f_m(\tau') \rangle = 2\bar{\gamma} \mathcal{D} \delta_{nm} \delta(\tau - \tau'), \quad \bar{\gamma} = \frac{\gamma}{\omega_*}. \quad (\text{S12})$$

with

$$\mathcal{D} = \frac{D_{\text{phys}}}{D_0}, \quad D_0 = mP_*^2\omega_*^2 = \frac{m\omega_0^4}{|\beta|}. \quad (\text{S13})$$

Thus \mathcal{D} is the dimensionless simulation noise intensity used in the numerical phase diagrams, whereas S_{noise} is the experimentally calibrated microwave noise spectral density. No equilibrium fluctuation–dissipation relation is assumed for the externally injected noise.

B. First-order state-space form

For the linear hybrid-carrier and Floquet branch-selection calculations, we use the homogeneous continuum model in k -space. With

$$\Phi(z, t) = \Phi_k(t) e^{ikz}, \quad Q(z, t) = Q_k(t) e^{ikz}, \quad P(z, t) = P_k(t) e^{ikz}, \quad (\text{S14})$$

the polarization stiffness becomes

$$\Omega_k^2(t) \equiv \Omega_0^2(t) + v_P^2 k^2.$$

Defining $\Pi \equiv m\dot{P}$ and using the canonical normalization convention $m\chi = 1$, we collect the variables as

$$\mathbf{a}(k, t) = \begin{bmatrix} \Phi \\ Q \\ P \\ \Pi \end{bmatrix}. \quad (\text{S15})$$

The linearized dynamics is

$$\frac{d}{dt} \mathbf{a}(k, t) = \mathbf{M}(k, t) \mathbf{a}(k, t), \quad (\text{S16})$$

with

$$\mathbf{M}(k, t) = \begin{bmatrix} 0 & \frac{1}{\varepsilon_b} & -\frac{1}{\varepsilon_b} & 0 \\ -\frac{k^2}{\mu} & 0 & 0 & 0 \\ 0 & 0 & 0 & \frac{1}{m} \\ 0 & \frac{1}{\varepsilon_b} & -m\Omega_k^2(t) - \frac{1}{\varepsilon_b} & -\gamma \end{bmatrix}. \quad (\text{S17})$$

The physical fields are recovered through

$$E_k = \frac{Q_k - P_k}{\varepsilon_b}, \quad H_k = -\frac{ik}{\mu}\Phi_k. \quad (\text{S18})$$

The Duffing nonlinearity is local in real space and appears in k -space as the convolution $[P^3]_k$. We therefore use Eq. (S17) only for the linear hybrid-carrier and Floquet branch-selection calculations; nonlinear saturation and stochastic dynamics are treated in the real-space lattice simulations.

C. Unmodulated hybrid carriers

The branch decomposition used below is defined by the unmodulated linear Maxwell–polarization problem. We set $\delta = 0$, $\beta = 0$, $F = 0$, and temporarily neglect damping. Harmonic solutions then satisfy

$$[\omega^2 - \omega_{\text{wg}}^2(k)] [\omega^2 - \omega_{\text{res}}^2(k)] = \omega_p^2 \omega^2, \quad (\text{S19})$$

with

$$\omega_{\text{wg}}^2(k) = \frac{k^2}{\mu\varepsilon_b}, \quad \omega_{\text{res}}^2(k) = \omega_0^2 + v_P^2 k^2, \quad \omega_p^2 = \frac{\chi}{\varepsilon_b} = \frac{1}{m\varepsilon_b}. \quad (\text{S20})$$

The last equality follows from the canonical normalization convention $m\chi = 1$. Equation (S19) gives two positive-frequency hybrid branches,

$$\omega_{\text{L,U}}^2(k) = \frac{1}{2} \left[\omega_{\text{wg}}^2(k) + \omega_{\text{res}}^2(k) + \omega_p^2 \mp \sqrt{[\omega_{\text{wg}}^2(k) + \omega_{\text{res}}^2(k) + \omega_p^2]^2 - 4\omega_{\text{wg}}^2(k)\omega_{\text{res}}^2(k)} \right], \quad (\text{S21})$$

where the minus sign gives the lower band $\omega_{\text{L}}(k)$ and the plus sign gives the upper band $\omega_{\text{U}}(k)$. In the weak-hybridization limit, the lower and upper bands reduce to the lower and upper of the two uncoupled dispersions,

$$\omega_{\text{L}}^2(k) \rightarrow \min\{\omega_{\text{wg}}^2(k), \omega_{\text{res}}^2(k)\}, \quad \omega_{\text{U}}^2(k) \rightarrow \max\{\omega_{\text{wg}}^2(k), \omega_{\text{res}}^2(k)\}. \quad (\text{S22})$$

On a discrete lattice, the corresponding bare dispersions are replaced by

$$\omega_{\text{wg}}^2(k) = \frac{4}{\mu\varepsilon_b d^2} \sin^2\left(\frac{kd}{2}\right), \quad \omega_{\text{res}}^2(k) = \omega_0^2 + 4g \sin^2\left(\frac{kd}{2}\right), \quad (\text{S23})$$

with $g = v_P^2/d^2$ in the central-difference convention used in Eq. (S10). The hybridization structure of Eq. (S19) is unchanged after replacing the bare dispersions by Eq. (S23).

D. Resonance conditions and selected carrier sectors

The driven normal form uses the unmodulated hybrid bands as carrier branches. We denote the lower and upper positive-frequency branches obtained in Eq. (S21) by

$$\omega_{\text{L}}(k), \quad \omega_{\text{U}}(k).$$

These bands are hybrid Maxwell–polarization modes: their electromagnetic and polarization contents vary with k , but the resonance conditions used below depend only on the carrier frequencies.

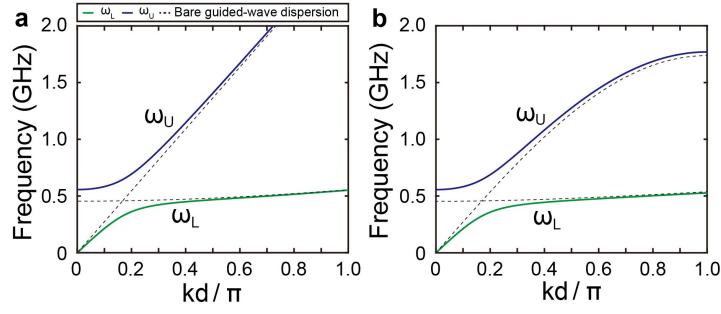


FIG. S1.1. **Unmodulated hybrid dispersion and resonance channels.** (a,b) Positive-frequency hybrid branches $\omega_L(k)$ and $\omega_U(k)$ obtained from the unmodulated Maxwell–Lorentz model in the continuum and discrete-lattice descriptions. Dashed curves show the uncoupled guided-wave and polarization dispersions. Markers indicate representative degenerate 2:1 and nondegenerate sum-resonant conditions used to define the DTC and DTQC carrier sectors.

Here k_0 denotes the resonant Bloch wave number, or the center of the narrow momentum window selected by the corresponding Floquet instability in a finite lattice. The two resonance classes central to the driven problem are first expressed at the level of these unmodulated bands. A degenerate 2:1 channel selects one band when

$$\Omega \simeq 2\omega_\nu(k_0), \quad \nu \in \{\text{L}, \text{U}\}. \quad (\text{S24})$$

This condition gives the single-branch DTC channels. By contrast, the nondegenerate sum-resonant channel selects one carrier from each band when

$$\Omega \simeq \omega_L(k_0) + \omega_U(k_0). \quad (\text{S25})$$

For a spatially uniform temporal modulation, momentum is conserved; in a real-field representation, Eq. (S25) corresponds to pairing opposite-momentum components $\pm k_0$ with the same band frequencies.

In the branch-reduced slow Hamiltonian used in the main text, the symbols a and b denote the selected near-resonant carrier sectors, not the full unmodulated bands. Thus, for the DTQC operating point,

$$\omega_a \simeq \omega_L(k_0), \quad \omega_b \simeq \omega_U(k_0), \quad (\text{S26})$$

whereas $\omega_{L,U}(k)$ denote the underlying unmodulated hybrid bands. The effective coefficients of the slow Hamiltonian are obtained by projecting the driven lattice dynamics onto these selected carrier sectors and retaining the near-resonant terms.

S2. CIRCUIT REALIZATION AND PROJECTED SLOW HAMILTONIAN

The experimental lattice is represented by a flux–charge circuit model. This formulation gives the element-level dictionary between the capacitances, inductances, varactor modulation, nonlinear charge response, and the projected slow-Hamiltonian coefficients used in the branch decomposition. We start from a bus node capacitively coupled to a nonlinear resonator node and then project the weakly time-dependent quadratic channels onto the hybrid carrier basis defined in Sec. S1.

A. Flux–charge circuit model

Each unit cell contains a bus node with flux $\Phi_n(t)$ and a resonator node with flux $\Psi_n(t)$. The corresponding node voltages are

$$V_{0,n} = \dot{\Phi}_n, \quad V_{r,n} = \dot{\Psi}_n. \quad (\text{S27})$$

The bus node is shunted by a capacitance C_0 , the bus and resonator nodes are coupled by a capacitance C_g , and the resonator node contains a time-modulated nonlinear capacitance. The resonator charge energy is written as

$$U_r(q_{r,n}; t) = \frac{q_{r,n}^2}{2C_{r,L}(t)} + \frac{q_{r,n}^4}{4C_{r,NL}}, \quad C_{r,L}(t) = \frac{C_{r,0}}{1 + \delta_r \cos(\Omega t)}. \quad (\text{S28})$$

The inductive network is separated into a guided bus sector and a resonator sector. The bus sector consists of the on-site shunt inductors L_s and nearest-neighbour series inductors L_0 , giving the discrete-gradient energy in Eq. (S31). The resonator sector consists of the resonator self-inductors L_r and a weak nearest-neighbour inductive coupling M . We define

$$k_r \equiv \frac{M}{L_r^2}, \quad (\text{S29})$$

and, to leading order in $M/L_r \ll 1$,

$$\mathbf{L}_r^{-1} = (L_r \mathbf{I} + M \mathbf{L}_2)^{-1} \simeq \frac{1}{L_r} \mathbf{I} - k_r \mathbf{L}_2, \quad (\text{S30})$$

where \mathbf{L}_2 is the second-difference discrete Laplacian.

We use a first-order flux–charge representation. Here Φ_n and Ψ_n are, respectively, the bus flux and resonator flux in the n -th unit cell. The branch charges $q_{0,n}$, $q_{g,n}$, and $q_{r,n}$ denote the charges on the bus capacitance C_0 , the bus–resonator coupling capacitor C_g , and the resonator varactor branch, respectively. The orientation of $q_{g,n}$ is chosen from the bus node to the resonator node, so that its first-order term is $q_{g,n}(\dot{\Phi}_n - \dot{\Psi}_n)$. The Lagrangian is then

$$\begin{aligned} \mathcal{L} = \sum_n \left[q_{0,n} \dot{\Phi}_n - \frac{q_{0,n}^2}{2C_0} + q_{g,n}(\dot{\Phi}_n - \dot{\Psi}_n) - \frac{q_{g,n}^2}{2C_g} + q_{r,n} \dot{\Psi}_n - U_r(q_{r,n}; t) \right] \\ - \sum_n \left[\frac{\Phi_n^2}{2L_s} + \frac{(\Phi_{n+1} - \Phi_n)^2}{2L_0} \right] - \frac{1}{2} \Psi^\top \mathbf{L}_r^{-1} \Psi. \end{aligned} \quad (\text{S31})$$

The canonical charges conjugate to Φ_n and Ψ_n are therefore

$$Q_{0,n} = q_{0,n} + q_{g,n}, \quad Q_{r,n} = q_{r,n} - q_{g,n}. \quad (\text{S32})$$

The independent circuit parameters entering Eqs. (S28), (S29), and (S31) are summarized in Table S1. The primed capacitances and effective modulation depths used below are derived from these bare circuit quantities.

TABLE S1. **Circuit parameters and modulation settings used in the flux–charge formulation.** The listed capacitances, inductances, coupling elements, nonlinearity scale, and drive settings define the circuit Hamiltonian in Sec. S2. Fixed entries are device parameters, whereas Ω and δ_r are selected for each operating branch. These quantities determine the effective capacitances, modulation depths, hybridization, Kerr coefficient, and phase stiffnesses entering the projected slow Hamiltonian.

Symbol	Meaning	Value	Unit
C_0	Bus-node shunt capacitance to ground	2.140×10^{-10}	F
C_g	Bus–resonator coupling capacitance	2.459×10^{-10}	F
$C_{r,0}$	Unmodulated linear resonator capacitance	1.070×10^{-10}	F
$C_{r,\text{NL}}$	Nonlinear-capacitance scale of the quartic resonator charge energy	1.225×10^{-30}	F C ²
Ω	Modulation frequency of the resonator capacitance	Branch-selected	rad/s
δ_r	Bare resonator-capacitance modulation depth in $C_{r,L}(t) = C_{r,0}/[1 + \delta_r \cos(\Omega t)]$	Swept	1
L_s	On-site bus shunt inductance	8.239×10^{-11}	H
L_0	Nearest-neighbour bus series inductance	4.120×10^{-12}	H
L_r	Resonator self-inductance	8.239×10^{-11}	H
M	Weak nearest-neighbour inductive coupling in the resonator sector	4.120×10^{-12}	H

B. Reduced capacitive Hamiltonian

Eliminating the internal capacitor charges gives the quadratic capacitive Hamiltonian

$$H_C(t) = \frac{1}{2} \sum_n [Q_{0,n} \quad Q_{r,n}] \mathbf{C}_{\text{eff}}^{-1}(t) \begin{bmatrix} Q_{0,n} \\ Q_{r,n} \end{bmatrix}. \quad (\text{S33})$$

At zero modulation, define

$$\Delta_0 = C_0 C_{r,0} + C_g (C_0 + C_{r,0}). \quad (\text{S34})$$

The static effective capacitances are

$$\frac{1}{C'_0} = \frac{C_g + C_{r,0}}{\Delta_0}, \quad \frac{1}{C'_r} = \frac{C_0 + C_g}{\Delta_0}, \quad \frac{1}{C'_g} = \frac{C_g}{\Delta_0}. \quad (\text{S35})$$

Thus

$$H_C^{(0)} = \sum_n \left[\frac{Q_{0,n}^2}{2C'_0} + \frac{Q_{r,n}^2}{2C'_r} + \frac{Q_{0,n}Q_{r,n}}{C'_g} \right]. \quad (\text{S36})$$

The nonlinear capacitor gives

$$H_{\text{NL}} = \sum_n \frac{q_{r,n}^4}{4C_{r,\text{NL}}}. \quad (\text{S37})$$

To leading order in the weak-loading expansion,

$$q_{r,n} \simeq \alpha_0 Q_{r,n} + \zeta_0 Q_{0,n}, \quad \alpha_0 = \frac{C_{r,0}(C_0 + C_g)}{\Delta_0}, \quad \zeta_0 = \frac{C_g C_{r,0}}{\Delta_0}, \quad (\text{S38})$$

so that

$$H_{\text{NL}} \simeq \sum_n \frac{(\alpha_0 Q_{r,n} + \zeta_0 Q_{0,n})^4}{4C_{r,\text{NL}}}. \quad (\text{S39})$$

C. Weak modulation and reduced circuit Hamiltonian

Expanding the inverse-capacitance matrix to first order in δ_r gives

$$\begin{aligned} \frac{1}{C'_r(t)} &\simeq \frac{1}{C'_r} [1 + \delta'_r \cos(\Omega t)], \\ \frac{1}{C'_g(t)} &\simeq \frac{1}{C'_g} [1 + \delta'_r \cos(\Omega t)], \\ \frac{1}{C'_0(t)} &\simeq \frac{1}{C'_0} [1 + \delta'_0 \cos(\Omega t)], \end{aligned} \quad (\text{S40})$$

where

$$\delta'_r = \delta_r \frac{C_{r,0}(C_0 + C_g)}{\Delta_0}, \quad \delta'_0 = \delta_r \frac{C_{r,0}C_g^2}{\Delta_0(C_g + C_{r,0})}. \quad (\text{S41})$$

The symbol δ_r denotes the bare resonator-capacitance modulation depth applied in the circuit. The quantities δ'_r and δ'_0 are the corresponding effective inverse-capacitance modulation depths after eliminating the internal capacitor charges. Because the resonator stiffness is proportional to the inverse capacitance, the Maxwell–Lorentz stiffness-modulation depth δ used in the main text should be interpreted as an effective modulation depth after this circuit reduction. When the resonator-sector stiffness modulation is used as the reference, we identify

$$\delta \equiv \delta_{\text{eff}} = \delta'_r. \quad (\text{S42})$$

The reduced circuit Hamiltonian becomes

$$\begin{aligned} H_{\text{circ}}(t) &= \sum_n \left[\frac{Q_{0,n}^2}{2C'_0} (1 + \delta'_0 \cos \Omega t) + \left(\frac{Q_{r,n}^2}{2C'_r} + \frac{Q_{0,n}Q_{r,n}}{C'_g} \right) (1 + \delta'_r \cos \Omega t) \right. \\ &\quad \left. + \frac{\Phi_n^2}{2L_s} + \frac{(\Phi_{n+1} - \Phi_n)^2}{2L_0} \right] + \frac{1}{2} \Psi^\top \mathbf{L}_r^{-1} \Psi + \sum_n \frac{(\alpha_0 Q_{r,n} + \zeta_0 Q_{0,n})^4}{4C_{r,\text{NL}}}. \end{aligned} \quad (\text{S43})$$

This Hamiltonian is the experimentally implemented discrete counterpart of the Maxwell–polarization model in Sec. S1. The bus coordinate Φ_n represents the guided-wave sector, while the resonator coordinate Ψ_n provides the dynamical polarization sector.

D. Two-sector slow variables

We introduce narrow-band action–angle variables in a frame rotating at $\Omega/2$. Let ω_{wg} and ω_r denote the selected unmodulated bus-like and resonator-like carrier frequencies. The corresponding complex amplitudes are

$$c_{0,n} = \sqrt{J_{0,n}} e^{-i\tilde{\theta}_{0,n}}, \quad c_{1,n} = \sqrt{J_{1,n}} e^{-i\tilde{\theta}_{1,n}}, \quad \tilde{\theta}_{\ell,n} = \theta_{\ell,n} - \frac{\Omega t}{2}. \quad (\text{S44})$$

The unmodulated number-conserving onsite quadratic sector is

$$\bar{H}_{\text{nc}}^{(2)} = \sum_n \begin{bmatrix} c_{0,n}^* & c_{1,n}^* \end{bmatrix} \begin{bmatrix} \Delta_{\text{wg}} & -G/2 \\ -G/2 & \Delta \end{bmatrix} \begin{bmatrix} c_{0,n} \\ c_{1,n} \end{bmatrix}, \quad (\text{S45})$$

with

$$\Delta_{\text{wg}} = \omega_{\text{wg}} - \frac{\Omega}{2}, \quad \Delta = \omega_r - \frac{\Omega}{2}. \quad (\text{S46})$$

The coupling scale G is inherited from the static bus–resonator capacitive coupling.

The weak modulation of the quadratic capacitive terms produces an effective bus-sector parametric coefficient h_{wg} , a resonator-sector coefficient h , and a modulation-induced inter-sector coefficient G_+ . The quadratic pump sector can be written as

$$\begin{aligned} \bar{H}_{\text{pump}}^{(2)} = & \sum_n \left[\frac{h_{\text{wg}}}{2} J_{0,n} \cos(2\tilde{\theta}_{0,n}) + \frac{h}{2} J_{1,n} \cos(2\tilde{\theta}_{1,n}) \right] \\ & - G_+ \sum_n \sqrt{J_{0,n} J_{1,n}} \cos(\tilde{\theta}_{0,n} + \tilde{\theta}_{1,n}). \end{aligned} \quad (\text{S47})$$

The onsite nonlinearity and spatial phase stiffnesses are summarized by

$$\bar{H}_{\text{Kerr}} = \sum_n \frac{\Lambda}{2} J_{1,n}^2, \quad (\text{S48})$$

and

$$\begin{aligned} \bar{H}_{\text{int}} = & - \sum_n K_{\text{wg}} \sqrt{J_{0,n} J_{0,n+1}} \cos(\tilde{\theta}_{0,n} - \tilde{\theta}_{0,n+1}) \\ & - \sum_n K \sqrt{J_{1,n} J_{1,n+1}} \cos(\tilde{\theta}_{1,n} - \tilde{\theta}_{1,n+1}). \end{aligned} \quad (\text{S49})$$

E. Hybrid basis and unified slow Hamiltonian

The unmodulated quadratic sector in Eq. (S45) is diagonalized by the real rotation

$$\begin{bmatrix} c_{0,n} \\ c_{1,n} \end{bmatrix} = \begin{bmatrix} \cos \psi & \sin \psi \\ -\sin \psi & \cos \psi \end{bmatrix} \begin{bmatrix} c_{a,n} \\ c_{b,n} \end{bmatrix}, \quad \tan(2\psi) = \frac{G}{\Delta_{\text{wg}} - \Delta}. \quad (\text{S50})$$

In this projected slow description, a and b label the two selected near-resonant carrier sectors drawn from the lower and upper hybrid bands. We define

$$c_{\alpha,n} = \sqrt{J_{\alpha,n}} e^{-i\tilde{\theta}_{\alpha,n}}, \quad \alpha \in \{a, b\}. \quad (\text{S51})$$

The hybrid detunings are

$$\Delta_{a,b} = \frac{\Delta_{\text{wg}} + \Delta}{2} \mp \sqrt{\left(\frac{\Delta_{\text{wg}} - \Delta}{2}\right)^2 + \left(\frac{G}{2}\right)^2}, \quad (\text{S52})$$

with hybrid carrier frequencies

$$\omega_{\alpha} = \Delta_{\alpha} + \frac{\Omega}{2}. \quad (\text{S53})$$

Projecting the quadratic pump sector onto the hybrid basis gives

$$\bar{H}_{\text{pump}}^{(2)} = \sum_n \left[\sum_{\alpha=a,b} \frac{h_\alpha}{2} J_{\alpha,n} \cos(2\tilde{\theta}_{\alpha,n}) - g_{ab} \sqrt{J_{a,n} J_{b,n}} \cos(\tilde{\theta}_{a,n} + \tilde{\theta}_{b,n}) \right], \quad (\text{S54})$$

where

$$\begin{aligned} h_a &= h_{\text{wg}} \cos^2 \psi + h \sin^2 \psi + G_+ \sin(2\psi), \\ h_b &= h_{\text{wg}} \sin^2 \psi + h \cos^2 \psi - G_+ \sin(2\psi), \\ g_{ab} &= \frac{h - h_{\text{wg}}}{2} \sin(2\psi) + G_+ \cos(2\psi). \end{aligned} \quad (\text{S55})$$

The Kerr and stiffness coefficients become

$$\Lambda_{aa} = \Lambda \sin^4 \psi, \quad \Lambda_{bb} = \Lambda \cos^4 \psi, \quad \Lambda_{ab} = 2\Lambda \sin^2 \psi \cos^2 \psi, \quad (\text{S56})$$

and

$$K_a = K_{\text{wg}} \cos^2 \psi + K \sin^2 \psi, \quad K_b = K_{\text{wg}} \sin^2 \psi + K \cos^2 \psi. \quad (\text{S57})$$

Off-diagonal gradient couplings are higher order in the narrow-band projection and are neglected at this order.

Collecting the projected terms gives the slow Hamiltonian used in the branch decomposition

$$\begin{aligned} \bar{\mathcal{H}} &= \sum_{n,\alpha=a,b} \left[\Delta_\alpha J_{\alpha,n} + \frac{\Lambda_{\alpha\alpha}}{2} J_{\alpha,n}^2 \right] + \sum_n \Lambda_{ab} J_{a,n} J_{b,n} \\ &\quad - \sum_{n,\alpha=a,b} K_\alpha \sqrt{J_{\alpha,n} J_{\alpha,n+1}} \cos(\tilde{\theta}_{\alpha,n} - \tilde{\theta}_{\alpha,n+1}) \\ &\quad + \sum_{n,\alpha=a,b} \frac{h_\alpha}{2} J_{\alpha,n} \cos(2\tilde{\theta}_{\alpha,n}) - g_{ab} \sum_n \sqrt{J_{a,n} J_{b,n}} \cos(\tilde{\theta}_{a,n} + \tilde{\theta}_{b,n}). \end{aligned} \quad (\text{S58})$$

The reduction is controlled when the envelope dynamics is slow on the carrier scale, so that

$$|\Delta_\alpha|, K_\alpha, h_\alpha, g_{ab} \sqrt{\bar{J}}, \Lambda_{\alpha\alpha} \bar{J}, \Lambda_{ab} \bar{J} \ll \Omega. \quad (\text{S59})$$

In this regime, nonsecular terms average out over many drive periods, and off-diagonal branch-gradient couplings are higher order in the narrow-band projection.

S3. BRANCH DECOMPOSITION: DEGENERATE DTC CHANNELS AND NONDEGENERATE DTQC CHANNEL

The unified slow Hamiltonian in Eq. (S58) contains the quadratic pump channels relevant to the driven lattice: two intraband degenerate locking terms proportional to h_a and h_b , and one interband sum-phase locking term proportional to g_{ab} . For the branch-reduced slow Hamiltonian, we use a and b to denote the two selected near-resonant carriers drawn from the lower and upper bands, respectively. Thus, in the DTQC channel, $\omega_a \simeq \omega_L(k_0)$ and $\omega_b \simeq \omega_U(k_0)$, while $\omega_{L,U}(k)$ denote the underlying unmodulated bands. These terms define the branch taxonomy used in the main text:

$$\text{DTC}_a : \Omega \simeq 2\omega_a, \quad \text{DTC}_b : \Omega \simeq 2\omega_b, \quad \text{DTQC} : \Omega \simeq \omega_a + \omega_b. \quad (\text{S60})$$

A. Linear Floquet branch landscape

The same resonance conditions appear in the time-periodic linearized dynamics as parametric-instability channels. At the level of the underlying unmodulated hybrid bands, degenerate pumping produces instability intervals near

$$2\omega_\nu(k) \simeq \Omega, \quad \nu \in \{L, U\}, \quad (\text{S61})$$

whereas the nondegenerate channel produces instability tongues near

$$\omega_L(k) + \omega_U(k) \simeq \Omega. \quad (\text{S62})$$

The former corresponds to excitation of a single hybrid band near half the pump frequency, whereas the latter corresponds to simultaneous excitation of one carrier from each band, with their sum phase locked to the drive.

Figure S1.1 defines the Maxwell–Lorentz lower and upper hybrid bands, whereas Fig. S3.1 shows how the corresponding instability channels are selected in the driven circuit realization. The two dispersions need not appear identical because the circuit guided-wave sector is a discrete LC network with a finite cutoff frequency; its bare dispersion bends near the Brillouin-zone edge instead of following an unbounded continuum light line. This cutoff modifies the hybridized band shapes and the resonant momentum windows while preserving the same lower/upper band structure. Panels (b–e) further include Floquet folding modulo Ω , so they display quasifrequencies $\text{Im}(\mu)/\Omega$ and growth rates $\text{Re}(\mu)/\Omega$ rather than the physical carrier frequency itself.

The selected carrier frequencies ω_a and ω_b used in the branch-reduced slow Hamiltonian are the near-resonant values drawn from these lower and upper bands. In the DTQC channel, for example, $\omega_a \simeq \omega_L(k_0)$ and $\omega_b \simeq \omega_U(k_0)$.

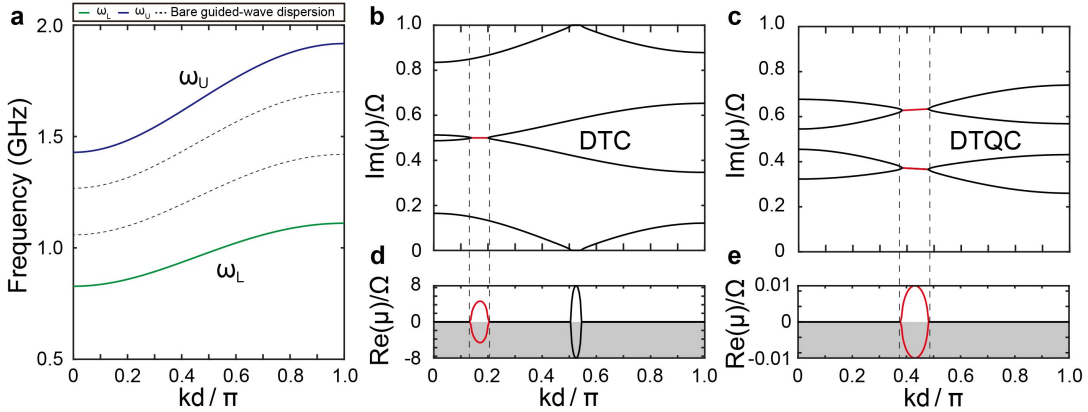


FIG. S3.1. **Floquet branch selection in the circuit realization.** (a) Unmodulated lower and upper hybrid bands $\omega_L(k)$ and $\omega_U(k)$ of the discrete guided-wave–resonator circuit model. The dotted curves show the bare guided-wave dispersions of the LC network, whose finite cutoff bends the branches at high momentum. (b,c) Floquet quasifrequencies $\text{Im}(\mu)/\Omega$ folded into the Floquet zone for the degenerate DTC and nondegenerate DTQC pumping conditions. Red segments and dashed vertical lines mark the selected near-resonant momentum windows. (d,e) Corresponding growth rates $\text{Re}(\mu)/\Omega$. Positive growth identifies parametrically unstable modes: the degenerate channels are selected near $2\omega_\nu(k) \simeq \Omega$, with $\nu \in \{L, U\}$, while the nondegenerate DTQC channel is selected near $\omega_L(k) + \omega_U(k) \simeq \Omega$. The selected near-resonant carrier frequencies from these windows are denoted by ω_a and ω_b in the branch-reduced slow Hamiltonian.

B. Branch I-A: DTC_a from $\Omega \simeq 2\omega_a$

The first degenerate channel is obtained by tuning the drive near the parametric resonance of hybrid branch a ,

$$\Omega = 2\omega_a + \Delta_{2,a}, \quad |\Delta_{2,a}| \ll \omega_a. \quad (\text{S63})$$

Equivalently, the rotating-frame detuning

$$\Delta_a = \omega_a - \frac{\Omega}{2} \quad (\text{S64})$$

is small. If the complementary branch is off resonant,

$$|\Delta_b| \gg \left\{ K_b, h_b, g_{ab}\sqrt{J} \right\}, \quad (\text{S65})$$

branch b can be eliminated to leading order. The effective Hamiltonian is

$$\bar{\mathcal{H}}_{\text{DTC},a} = \sum_n \left[\Delta_a J_{a,n} + \frac{\Lambda_{aa}}{2} J_{a,n}^2 + \frac{h_a}{2} J_{a,n} \cos(2\tilde{\theta}_{a,n}) \right] - \sum_n K_a \sqrt{J_{a,n} J_{a,n+1}} \cos(\tilde{\theta}_{a,n} - \tilde{\theta}_{a,n+1}). \quad (\text{S66})$$

The term proportional to h_a pins $2\tilde{\theta}_{a,n}$ and produces two symmetry-related subharmonic phase sectors. In the driven-dissipative dynamics, damping and nonlinear saturation convert this parametric instability into a period-doubled attractor.

C. Branch I-B: DTC_b from $\Omega \simeq 2\omega_b$

The second degenerate channel is obtained by tuning the drive near the parametric resonance of hybrid branch b ,

$$\Omega = 2\omega_b + \Delta_{2,b}, \quad |\Delta_{2,b}| \ll \omega_b. \quad (\text{S67})$$

The rotating-frame detuning

$$\Delta_b = \omega_b - \frac{\Omega}{2} \quad (\text{S68})$$

is then small. If branch a is off resonant,

$$|\Delta_a| \gg \left\{ K_a, h_a, g_{ab}\sqrt{J} \right\}, \quad (\text{S69})$$

the slow Hamiltonian reduces to

$$\bar{\mathcal{H}}_{\text{DTC},b} = \sum_n \left[\Delta_b J_{b,n} + \frac{\Lambda_{bb}}{2} J_{b,n}^2 + \frac{h_b}{2} J_{b,n} \cos(2\tilde{\theta}_{b,n}) \right] - \sum_n K_b \sqrt{J_{b,n} J_{b,n+1}} \cos(\tilde{\theta}_{b,n} - \tilde{\theta}_{b,n+1}). \quad (\text{S70})$$

In the weak-mixing limit, branch b is predominantly resonator-like, with $\omega_b \rightarrow \omega_r$, $h_b \rightarrow h$, $K_b \rightarrow K$, and $\Lambda_{bb} \rightarrow \Lambda$. This is the branch most directly connected to the polarization-sector period-doubling mechanism.

D. Branch II: DTQC from $\Omega \simeq \omega_a + \omega_b$

The DTQC branch is selected by the nondegenerate sum resonance

$$\Omega \simeq \omega_a + \omega_b. \quad (\text{S71})$$

In the $\Omega/2$ rotating frame, this is equivalent to

$$\Delta_a + \Delta_b \simeq 0. \quad (\text{S72})$$

Near this condition, the dominant resonant pump channel is the interbranch term proportional to g_{ab} . The intrabranch 2:1 terms proportional to h_a and h_b are off resonant in this nondegenerate sum-resonant branch and are therefore omitted from the branch-reduced DTQC Hamiltonian. If an additional low-order commensurability brought either intrabranch term into resonance, it would provide an extra phase-locking channel and could collapse the torus into a finite-period orbit. The effective two-branch Hamiltonian is

$$\begin{aligned} \bar{\mathcal{H}}_{\text{DTQC}} = & \sum_n \left[\Delta_a J_{a,n} + \Delta_b J_{b,n} + \frac{\Lambda_{aa}}{2} J_{a,n}^2 + \frac{\Lambda_{bb}}{2} J_{b,n}^2 + \Lambda_{ab} J_{a,n} J_{b,n} \right] \\ & - \sum_n K_a \sqrt{J_{a,n} J_{a,n+1}} \cos(\tilde{\theta}_{a,n} - \tilde{\theta}_{a,n+1}) \\ & - \sum_n K_b \sqrt{J_{b,n} J_{b,n+1}} \cos(\tilde{\theta}_{b,n} - \tilde{\theta}_{b,n+1}) \\ & - g_{ab} \sum_n \sqrt{J_{a,n} J_{b,n}} \cos(\tilde{\theta}_{a,n} + \tilde{\theta}_{b,n}). \end{aligned} \quad (\text{S73})$$

The last term pins the slow sum phase

$$\Theta_{+,n} = \tilde{\theta}_{a,n} + \tilde{\theta}_{b,n}, \quad (\text{S74})$$

while the complementary phase

$$\Theta_{-,n} = \tilde{\theta}_{a,n} - \tilde{\theta}_{b,n} \quad (\text{S75})$$

is not directly pinned by the pump. Consequently, the local nonlinear attractor is a two-frequency torus rather than a period-doubled limit cycle. In the coupled lattice, the spatial stiffness terms promote coherent locking of $\Theta_{+,n}$ across sites while allowing $\Theta_{-,n}$ to wind, producing the DTQC response discussed in the main text.

E. Frozen-action phase reduction and deterministic sum-locking tongue

This subsection derives the phase-reduced locking estimate used in the main text. The purpose of the estimate is limited: it identifies the deterministic sum-phase locking tongue of the branch-reduced normal form. It is not an exact phase boundary of the full driven-dissipative Maxwell-polarization lattice.

We first suppress the site index and retain the local part of Eq. (S73),

$$\bar{\mathcal{H}}_{\text{loc}} = \Delta_a J_a + \Delta_b J_b + \frac{\Lambda_{aa}}{2} J_a^2 + \frac{\Lambda_{bb}}{2} J_b^2 + \Lambda_{ab} J_a J_b - g_{ab} \sqrt{J_a J_b} \cos \Theta_+, \quad \Theta_+ = \tilde{\theta}_a + \tilde{\theta}_b. \quad (\text{S76})$$

This expression assumes the nondegenerate sum-resonant sector, so the intrabranch 2:1 locking terms are off resonant or small compared with the retained sum-resonant channel. Uniform contributions from the spatial stiffness are absorbed into the renormalized rotating-frame detunings Δ_α .

Hamilton's equations give

$$\begin{aligned} \dot{\tilde{\theta}}_a &= \Delta_a + \Lambda_{aa} J_a + \Lambda_{ab} J_b - \frac{g_{ab}}{2} \sqrt{\frac{J_b}{J_a}} \cos \Theta_+, \\ \dot{\tilde{\theta}}_b &= \Delta_b + \Lambda_{bb} J_b + \Lambda_{ab} J_a - \frac{g_{ab}}{2} \sqrt{\frac{J_a}{J_b}} \cos \Theta_+. \end{aligned} \quad (\text{S77})$$

Adding the two equations yields

$$\dot{\Theta}_+ = \Delta_a + \Delta_b + \Lambda_{aa} J_a + \Lambda_{bb} J_b + \Lambda_{ab} (J_a + J_b) - \frac{g_{ab}}{2} \left(\sqrt{\frac{J_b}{J_a}} + \sqrt{\frac{J_a}{J_b}} \right) \cos \Theta_+. \quad (\text{S78})$$

For a spatially coherent saturated state with finite actions $J_a = \bar{J}_a > 0$ and $J_b = \bar{J}_b > 0$, this becomes the frozen-action Adler-type equation

$$\dot{\Theta}_+ = \Delta_+^{\text{eff}} - W_+ \cos(\Theta_+ - \Theta_0) + \dots, \quad (\text{S79})$$

with

$$\Delta_+^{\text{eff}} = \Delta_a + \Delta_b + \Lambda_{aa} \bar{J}_a + \Lambda_{bb} \bar{J}_b + \Lambda_{ab} (\bar{J}_a + \bar{J}_b), \quad (\text{S80})$$

and

$$W_+ = \frac{|g_{ab}|}{2} \left(\sqrt{\frac{\bar{J}_b}{\bar{J}_a}} + \sqrt{\frac{\bar{J}_a}{\bar{J}_b}} \right). \quad (\text{S81})$$

The phase offset Θ_0 absorbs the sign and phase convention of the pump-induced coupling. The notation W_+ is used to emphasize that this quantity is a locking bandwidth in the reduced phase equation, not a damping rate. The local restoring rate near a stable fixed point is proportional to

$$\lambda_+ \sim \sqrt{W_+^2 - (\Delta_+^{\text{eff}})^2}, \quad (\text{S82})$$

up to dissipative and saturation-dependent renormalizations.

A deterministic sum-locked fixed point of Eq. (S79) can exist only when

$$|\Delta_+^{\text{eff}}| \leq W_+. \quad (\text{S83})$$

This condition is necessary at the level of the frozen-action deterministic phase reduction. It is not sufficient for a DTQC state. The full DTQC window additionally requires stable nonlinear saturation of both branch actions, transverse stability of the resulting torus, spatial coherence of the locked sum phase, absence of low-order complementary-phase locking, and a restoring rate or slip barrier large enough to overcome noise-induced dephasing. These additional requirements are precisely the quantities tested in the numerical and experimental diagnostics in the main text.

The apparent divergence of W_+ as $\bar{J}_a \rightarrow 0$ or $\bar{J}_b \rightarrow 0$ is a coordinate singularity of the action-angle phase reduction. The underlying coupling energy $|g_{ab}| \sqrt{\bar{J}_a \bar{J}_b}$ vanishes when either branch amplitude vanishes. Therefore Eqs. (S79)–(S83) are used only in the saturated two-branch regime with finite \bar{J}_a and \bar{J}_b .

F. Slow-flow equations and noise projection

The deterministic branch-reduced dynamics follows from Hamilton's equations,

$$\dot{J}_{\alpha,n} = -\frac{\partial \bar{\mathcal{H}}}{\partial \tilde{\theta}_{\alpha,n}}, \quad \dot{\tilde{\theta}}_{\alpha,n} = \frac{\partial \bar{\mathcal{H}}}{\partial J_{\alpha,n}}, \quad \alpha \in \{a, b\}. \quad (\text{S84})$$

Damping and noise are obtained by projecting the polarization-sector Langevin dynamics onto the slow variables. In the numerical implementation, this projection is represented by effective branch-resolved damping and calibrated slow-noise terms,

$$\begin{aligned} \dot{J}_{\alpha,n} &= -\frac{\partial \bar{\mathcal{H}}}{\partial \tilde{\theta}_{\alpha,n}} - \Gamma_{\alpha}^{(J)}(J_{\alpha,n} - J_{\alpha,n}^{\text{ss}}) + \xi_{\alpha,n}^{(J)}(t), \\ \dot{\tilde{\theta}}_{\alpha,n} &= \frac{\partial \bar{\mathcal{H}}}{\partial J_{\alpha,n}} + \xi_{\alpha,n}^{(\theta)}(t). \end{aligned} \quad (\text{S85})$$

The effective noise strength appearing in the numerical phase diagrams is denoted by \mathcal{D} . It is the dimensionless slow-variable noise scale obtained by nondimensionalizing the lattice-level Langevin convention in Eq. (S11), as summarized in Eqs. (S12) and (S13).

The activation-barrier analysis used in Figs. 2(d,g) and 3(g) is performed from rare phase-slip statistics in the noisy slow-flow simulations. In the DTC sector, the pinned variable is $2\tilde{\theta}_{\alpha}$, so slips are identified from π jumps of the continuously lifted resonant rotating-frame phase $\tilde{\theta}_{\alpha}$. In the DTQC sector, slips are identified from 2π jumps of the continuously lifted locked sum phase Θ_{+} . Short-time fluctuations are removed before slip counting. The switching rate Γ is estimated from the number of completed slips divided by the total post-transient exposure time. For each N , the effective activation barrier E_A is extracted from a linear fit of $\ln \Gamma$ versus $1/\mathcal{D}$ over the rare-slip regime.

For the DTQC branch, the useful phase variables are $\Theta_{+,n}$ and $\Theta_{-,n}$. From Eq. (S73), the sum-resonant coupling contributes

$$\dot{J}_{a,n}|_{g_{ab}} = -g_{ab}\sqrt{J_{a,n}J_{b,n}}\sin\Theta_{+,n}, \quad \dot{J}_{b,n}|_{g_{ab}} = -g_{ab}\sqrt{J_{a,n}J_{b,n}}\sin\Theta_{+,n}, \quad (\text{S86})$$

and

$$\dot{\tilde{\theta}}_{a,n}|_{g_{ab}} = -\frac{g_{ab}}{2}\sqrt{\frac{J_{b,n}}{J_{a,n}}}\cos\Theta_{+,n}, \quad \dot{\tilde{\theta}}_{b,n}|_{g_{ab}} = -\frac{g_{ab}}{2}\sqrt{\frac{J_{a,n}}{J_{b,n}}}\cos\Theta_{+,n}. \quad (\text{S87})$$

These equations make explicit that the pump acts on the sum phase, while the complementary phase remains the winding phase of the quasiperiodic motion.

G. Validation against the full time-domain model

The branch-reduced Hamiltonians are validated by comparison with direct time-domain integration of the full Maxwell–Lorentz equations. The comparison is performed at a representative probe site by extracting the branch actions and slow phases from the full time-domain signal and comparing them with the corresponding slow-flow variables. Figure S3.2 shows that the reduced variables reproduce the slow envelopes and phases of the full dynamics in the two degenerate DTC channels and in the nondegenerate DTQC channel. The agreement supports using Eq. (S66), Eq. (S70), and Eq. (S73) as the branch-resolved normal forms in the remainder of the analysis.

Branch I consists of the two degenerate parametric resonance channels DTC_a and DTC_b , realized near $\Omega \simeq 2\omega_a$ and $\Omega \simeq 2\omega_b$, respectively. Branch II is the nondegenerate sum-resonant DTQC channel, realized near $\Omega \simeq \omega_a + \omega_b$. In the weak-mixing limit, these hybrid-branch conditions reduce continuously to the corresponding bare-sector conditions.

S4. EXPERIMENTAL IMPLEMENTATION

A. Experimental platform, measurement setup, and noise injection

To implement the unit cell of the nonlinear LC resonator, a metallic split-ring resonator (SRR) was patterned onto a printed circuit board (Fig. S4.1b). Each unit cell incorporates a varactor diode (SMV1247, Skyworks), whose

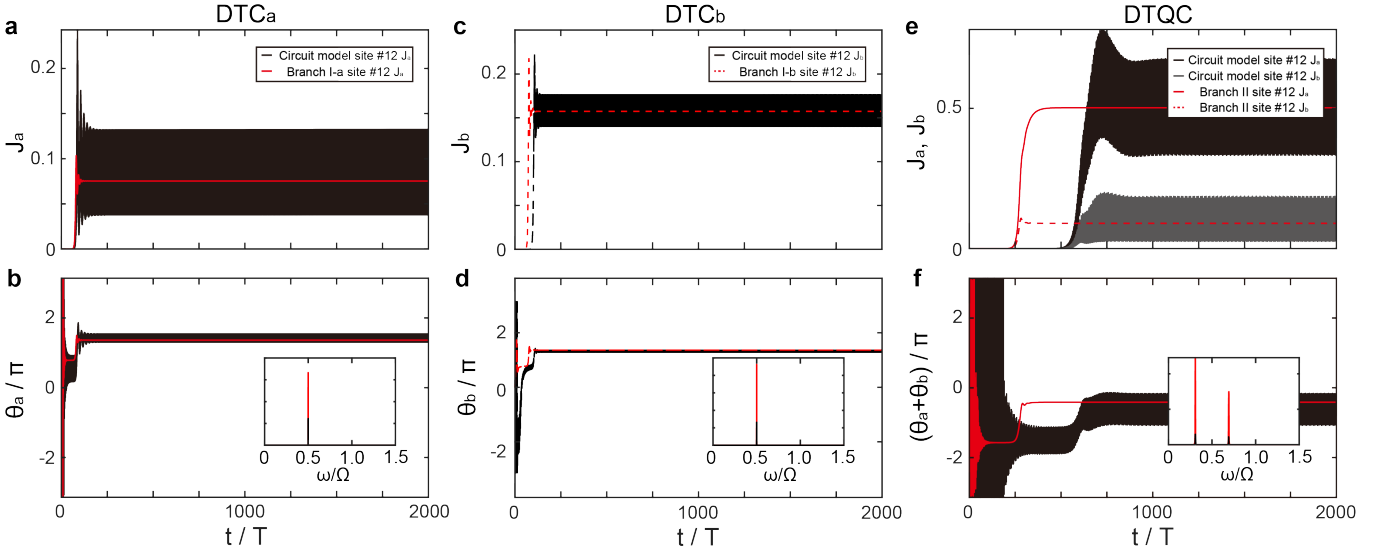


FIG. S3.2. **Validation of branch-reduced slow-flow dynamics.** Black traces show quantities extracted from direct numerical integration of the full circuit equations of motion, while red traces show the corresponding branch-reduced slow-flow results. The time axis is normalized by the drive period $T = 2\pi/\Omega$. (a,b) DTC_a: action J_a and slow phase $\tilde{\theta}_a$. (c,d) DTC_b: action J_b and slow phase $\tilde{\theta}_b$. (e,f) DTQC: actions (J_a, J_b) and the slow sum phase $(\tilde{\theta}_a + \tilde{\theta}_b)/\pi$. Insets show normalized spectra of the corresponding probe signal, confirming the single-frequency DTC response and the two-frequency DTQC response captured by the branch-reduced normal forms.

capacitance can be modulated by applying a DC-biased AC voltage across it. As a result, the resonant characteristics of the unit cell undergo time-periodic modulation. In the experiment, a DC bias voltage of 2.6 V is applied. The discrete time-crystalline (DTC) phase is observed at $\Omega = 2\pi f_{\text{mod}}$ with $f_{\text{mod}} = 2.98$ GHz, while the discrete time-quasicrystalline (DTQC) phase is observed at $\Omega = 2\pi f_{\text{mod}}$ with $f_{\text{mod}} = 2.47$ GHz.

To construct a one-dimensional array of coupled nonlinear LC resonators, 12 unit cells were placed inside a waveguide (Fig. S4.1a). The complete experimental setup is shown in Fig. S4.1c. The driving signal (AC voltage) is generated by a signal generator (N5171B, Keysight) and amplified by a radio-frequency amplifier (RUM43020-10, RFHIC). The amplified AC voltage is then DC-biased using a bias tee and subsequently distributed through a two-way splitter, followed by a six-way splitter. Additional two-way splitters are inserted just before the resonator array, with each splitter enabling individual signal measurement from a corresponding unit cell. To prevent unwanted DC current flow, a DC block is inserted at one end of the two-way splitter. Additionally, a low-pass filter (LPF) is placed before the oscilloscope (DPO 70804, Tektronix) or spectrum analyzer (E4404B, Agilent) to suppress reflections of the driving signal. The radio-frequency modulation distributed by the splitter network is the only coherent external temporal drive. Fixed cable delays and splitter phases correspond to static phase offsets of the same global tone and do not introduce an additional modulation frequency.

Noise is injected from one end of the waveguide using a noise source module (PE85N1012, Pasternack), which generates broadband noise in the 10 MHz to 3 GHz range. This noise is further amplified by a high-power amplifier (ZHL-10W-202-S+, Mini-Circuits). A variable attenuator (PE7422, Pasternack) is used to control the noise intensity injected into the system. Fig. S4.2 shows the power spectrum of the noise source measured before entering the waveguide, with a 30 dB variable attenuator applied. The amplifier operates over a frequency range of 10 MHz to 2 GHz, within which the power level is approximately -93.34 dBm/Hz. This value is used in the main text as a reference for characterizing the noise power spectral density. The injected noise is broadband and phase-incoherent; it does not supply a coherent temporal lattice vector or a second imposed clock. Its role is to seed fluctuations and tune phase-slip statistics, while the response frequencies and the locked sum phase are selected by the driven nonlinear lattice.

B. Signal processing and reconstruction of experimental DTQC observables

The experimental DTQC observables in Fig. 3(i-k,n) are reconstructed from the measured cell-resolved voltage traces $V_n(t)$. The measured-site set is the simultaneously recorded four-channel set $\mathcal{M} = \{7, 8, 9, 10\}$, with $N_{\mathcal{M}} =$

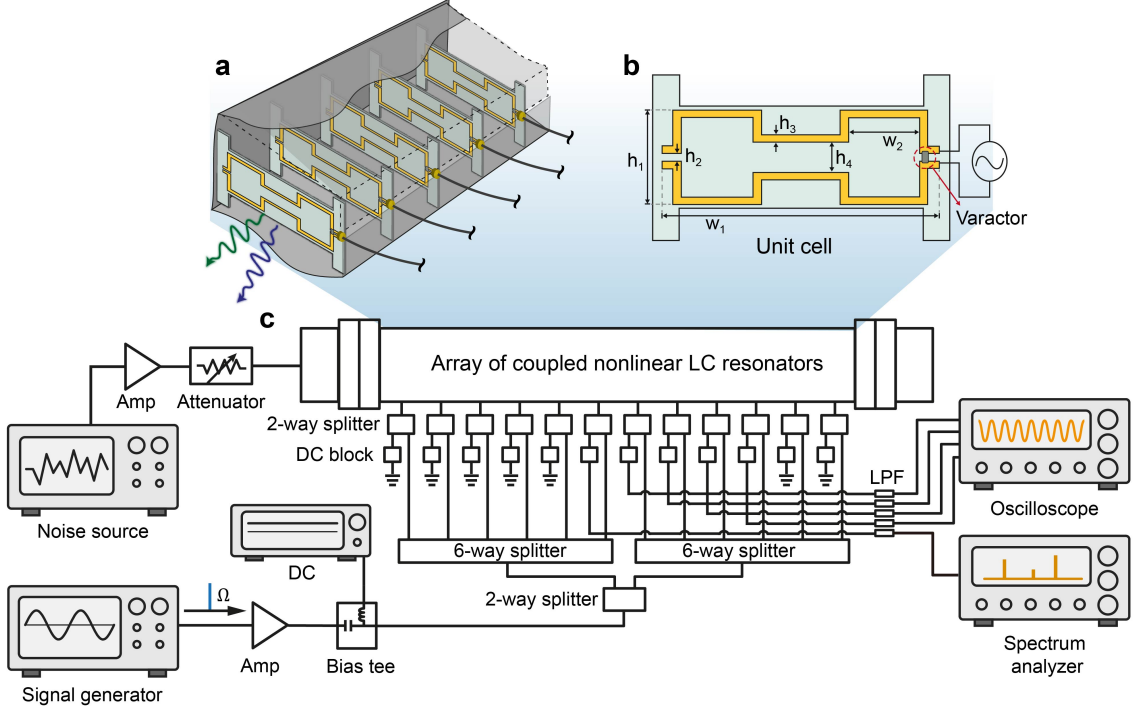


FIG. S4.1. **Experimental platform: modulated nonlinear LC-resonator array in a waveguide.** (a) Schematic of a one-dimensional array of $N = 12$ coupled nonlinear LC resonators embedded in a waveguide. (b) Geometry of a single unit cell incorporating a varactor diode that enables time-periodic modulation of the capacitance via an AC drive voltage applied on top of a DC bias. The unit-cell dimensions are $h_1 = 40$ mm, $h_2 = 1$ mm, $h_3 = 3$ mm, $h_4 = 10$ mm, $w_1 = 105$ mm, and $w_2 = 27.5$ mm. (c) Block diagram of the experimental measurement setup used to drive the modulation and record the waveguide response.

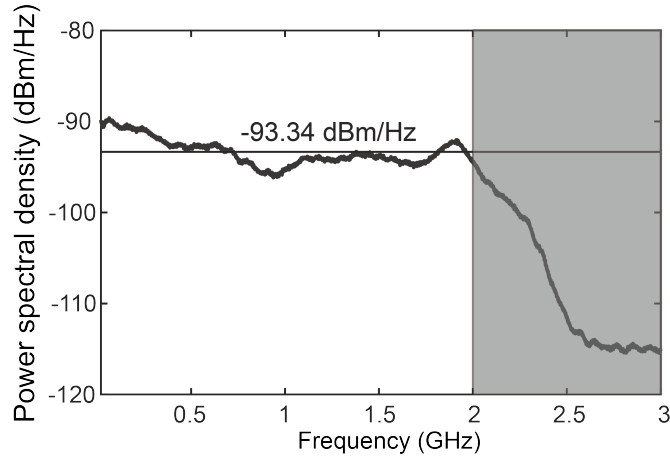


FIG. S4.2. **Characterization of the injected noise spectrum.** Power spectral density of the external noise source measured before injection into the waveguide, using a 30 dB attenuator. The mean level over the 10 MHz–2 GHz band is approximately -93.34 dBm/Hz, which is used as the reference noise power spectral density in the experiments.

$|\mathcal{M}| = 4$, and the representative-site phase reconstruction in Fig. 3(k) is shown for $n_0 = 7$. The DTQC data are analyzed at the modulation frequency $f_{\text{mod}} = \Omega/2\pi = 2.47$ GHz, using the original oscilloscope time grid at 25 GSa/s.

For each measured site n , we compute the steady-state voltage spectrum and identify the two dominant peaks associated with the DTQC response using a fixed peak-selection criterion applied uniformly across the measured data set.

For the experimental phase diagram, the spectral proxy is evaluated from the two peak heights

$$M_{\text{DTQC}}^{\text{spec}} = \left(A_1^{\text{pk}} A_2^{\text{pk}} \right)^{1/2}. \quad (\text{S88})$$

Here A_j^{pk} denotes the peak height of the steady-state voltage spectrum in the fixed frequency window assigned to the j -th DTQC response component. The same peak windows and peak-extraction procedure are applied to all operating points in the (S_{noise}, P_d) scan. We use the peak levels directly and apply the same fixed-window extraction protocol to every operating point, so that $M_{\text{DTQC}}^{\text{spec}}$ consistently tracks the joint appearance of the two DTQC response peaks.

When the spectra are displayed in logarithmic power units, the displayed proxy is written as

$$M_{\text{DTQC}}^{\text{spec}}[\text{dBm}] = \frac{P_1^{\text{pk}}[\text{dBm}] + P_2^{\text{pk}}[\text{dBm}]}{2}, \quad (\text{S89})$$

which is the logarithmic representation of the geometric mean of the corresponding linear peak powers.

Throughout the phase reconstruction and quasiperiodicity analysis we use angular frequencies. At the representative operating point marked in Fig. 3(h) and shown in Fig. 3(i-k), the selected response frequencies and the imposed modulation frequency are

$$\frac{\omega_1}{2\pi} = 0.966 \text{ GHz}, \quad \frac{\omega_2}{2\pi} = 1.50 \text{ GHz}, \quad \frac{\Omega}{2\pi} = 2.47 \text{ GHz}. \quad (\text{S90})$$

The selected pair (ω_1, ω_2) defines the two narrow-band voltage components used for phase extraction and for the quasiperiodicity diagnostics in Fig. 4. The numerical values in Eq. (S90) are rounded for display; the phase reconstruction and low-order diagnostics use the extracted frequencies before rounding.

From the two corresponding narrow-band voltage components, we construct analytic signals

$$\mathcal{A}_n^{(j)}(t) = V_n^{(j)}(t) + i \text{H} \left[V_n^{(j)}(t) \right], \quad j = 1, 2, \quad (\text{S91})$$

where H denotes the Hilbert transform. We write

$$\mathcal{A}_n^{(j)}(t) = R_{j,n}(t) e^{i\phi_{j,n}(t)}, \quad R_{j,n}(t) > 0, \quad (\text{S92})$$

with $\phi_{j,n}(t)$ chosen continuously over the post-transient analysis window. To use the same rotating-frame convention as the branch-reduced normal form, we define

$$\tilde{\phi}_{j,n}(t) = \phi_{j,n}(t) - \frac{\Omega t}{2}, \quad j = 1, 2. \quad (\text{S93})$$

For the representative site $n_0 = 7$, the reconstructed sum phase is defined modulo 2π as

$$\Theta_{+,n_0}(t) = \tilde{\phi}_{1,n_0}(t) + \tilde{\phi}_{2,n_0}(t) \pmod{2\pi}, \quad (\text{S94})$$

and the complementary phase is kept as a continuous winding coordinate,

$$\Theta_{-,n_0}(t) = \tilde{\phi}_{1,n_0}(t) - \tilde{\phi}_{2,n_0}(t). \quad (\text{S95})$$

Equivalently,

$$\Theta_{+,n_0}(t) = \phi_{1,n_0}(t) + \phi_{2,n_0}(t) - \Omega t \pmod{2\pi}, \quad \Theta_{-,n_0}(t) = \phi_{1,n_0}(t) - \phi_{2,n_0}(t). \quad (\text{S96})$$

The sum phase Θ_{+,n_0} diagnoses locking of the two-frequency response to the imposed pump, whereas Θ_{-,n_0} is the winding phase of the unpinned complementary degree of freedom. Figure 3(k) is obtained by plotting these two quantities for the representative-site voltage trace used in Fig. 3(i,j).

The two-phase trajectory shown in Fig. 4(c) and the recurrence diagnostic in Fig. 4(d) are reconstructed from the same representative-site signal using the same half-pump rotating phase coordinates $(\tilde{\phi}_{1,n_0}, \tilde{\phi}_{2,n_0})$. Their quantitative definitions are given in Sec. S4C.

The measured-site coherence shown in Fig. 3(n) is the measured-site specialization of the main-text complex phase memory, evaluated from the locked sum phase,

$$Z_{\Theta_+}^{(\mathcal{M})}(t) \equiv \frac{1}{N_{\mathcal{M}}} \sum_{n \in \mathcal{M}} e^{i\Delta\Theta_{+,n}(t)}, \quad \Delta\Theta_{+,n}(t) = \Theta_{+,n}(t) - \Theta_{+,n}(t_{\text{ref}}) \pmod{2\pi}. \quad (\text{S97})$$

Here t_{ref} is the first time point of the post-transient analysis window, and the plotted scalar coherence is $|Z_{\Theta_+}^{(\mathcal{M})}(t)|$. Because a finite number of sites gives a nonzero coherence even for random phases, we compare $|Z_{\Theta_+}^{(\mathcal{M})}(t)|$ with a finite-site random-phase reference computed for the same $N_{\mathcal{M}} = 4$. The 95% baseline is obtained from 4000 independent random-phase realizations, and the plotted null reference is the 95th percentile of the resulting finite-site distribution.

For comparison with simulations, we evaluate the same complex phase memory $Z_{\Theta_+}^{(\mathcal{S})}(t)$ in an $N = 12$ coupled array, both over the full array and over the representative four-site subset $\mathcal{S} = \mathcal{M} = \{7, 8, 9, 10\}$. The same number of random-phase realizations (4000) is used for the finite-site null baseline, and the time-averaged quantities are extracted after a burn-in window of $50T$. Thus the measured voltages and spectrum in Fig. 3(i,j), the representative-site phase reconstruction in Fig. 3(k), the measured-site coherence in Fig. 3(n), and the quasiperiodicity diagnostics in Fig. 4 are all defined from a common signal-processing pipeline.

C. Quantitative quasiperiodicity diagnostics for the experimental DTQC state

The quasiperiodicity diagnostics in Fig. 4 are evaluated at the same representative operating point and from the same selected angular-frequency pair (ω_1, ω_2) used for the phase reconstruction and measured-site coherence analysis in Sec. S4B. These diagnostics test whether the observed two-frequency response is consistent with a quasiperiodic DTQC state, rather than with simple low-order locking to the single imposed modulation.

We first test small-integer relations among the two response frequencies and the imposed modulation frequency. For each integer pair (l_1, l_2) , we define the normalized low-order mismatch

$$\Delta_{l_1, l_2} = \min_{l_3 \in \mathbb{Z}} \frac{|l_1 \omega_1 + l_2 \omega_2 - l_3 \Omega|}{\Omega}. \quad (\text{S98})$$

Equivalently, l_3 is chosen as the nearest integer to $(l_1 \omega_1 + l_2 \omega_2)/\Omega$. In the relation map shown in Fig. 4(a), the integer pair (l_1, l_2) is restricted to a finite low-order window, excluding the trivial zero vector. For Fig. 4(a), we use $|l_1|, |l_2| \leq L_{\text{max}}$ with $L_{\text{max}} = 8$. The low-mismatch diagonal corresponds to integer multiples of the expected sum-resonant condition

$$\omega_1 + \omega_2 \simeq \Omega, \quad (\text{S99})$$

whereas additional low-order frequency locking would appear as other isolated low-mismatch points away from this sum-resonant family. Within the experimental frequency resolution, no such additional low-order relation is observed.

The combination-line overlay in Fig. 4(b) is constructed from the same two extracted angular frequencies. Candidate spectral lines are generated as

$$\omega_{m, n} = m\omega_1 + n\omega_2, \quad m, n \in \mathbb{Z}, \quad (\text{S100})$$

and only positive frequencies inside the plotted spectral window are retained. In practice, the displayed set is restricted to low-order combinations. For Fig. 4(b), we retain combinations satisfying $|m| + |n| \leq M_{\text{max}}$ with $M_{\text{max}} = 4$. This construction does not introduce additional fitting frequencies; it tests whether the measured spectrum is organized by the same two fundamentals used in the phase reconstruction.

For the two-phase reconstruction in Fig. 4(c), we use the half-pump rotating phases modulo 2π ,

$$\left(\tilde{\phi}_{1, n_0}(t) \bmod 2\pi, \tilde{\phi}_{2, n_0}(t) \bmod 2\pi \right) \in \mathbb{T}^2, \quad (\text{S101})$$

where $\tilde{\phi}_{j, n}$ is defined in Eq. (S93). This two-phase representation is not the full Hamiltonian phase space of the driven lattice; rather, it is a signal-level projection of the measured voltage response onto the two extracted DTQC components in the same half-pump rotating convention used for the branch-reduced normal form. The same coordinates are used for the recurrence diagnostic in Fig. 4(d).

Finally, we quantify recurrence of the reconstructed two-phase trajectory by computing a minimum return distance on the half-pump rotating phase torus. For a time lag τ , we define

$$d_{\min}(\tau) = \min_{t \in \mathcal{W}_\tau} \frac{1}{\sqrt{2\pi}} \left[d_{\mathbb{T}}^2 \left(\tilde{\phi}_{1, n_0}(t + \tau), \tilde{\phi}_{1, n_0}(t) \right) + d_{\mathbb{T}}^2 \left(\tilde{\phi}_{2, n_0}(t + \tau), \tilde{\phi}_{2, n_0}(t) \right) \right]^{1/2}, \quad (\text{S102})$$

where \mathcal{W}_τ is the post-transient analysis window for which both t and $t + \tau$ lie inside the measured trace, and

$$d_{\mathbb{T}}(\phi, \phi') = \min_{m \in \mathbb{Z}} |\phi - \phi' + 2\pi m|. \quad (\text{S103})$$

is the wrapped phase distance on the circle. For Fig. 4(d), lags shorter than $\tau_{\text{excl}} = 10T$ are excluded to avoid trivial continuity-induced returns. A strictly low-order periodic orbit would exhibit near-zero return distances at its closure time. By contrast, the experimental trajectory shows only finite-time near returns over the accessible observation window, without low-order exact closure. This recurrence diagnostic does not constitute a mathematical proof of irrationality, but it provides a quantitative finite-time test against a simple weak-locking interpretation.

Taken together, the low-order integer-relation test, the two-frequency combination spectrum, the half-pump rotating two-phase reconstruction, and the recurrence analysis support the interpretation of the observed response as a quasiperiodic DTQC state rather than a low-order frequency-locked periodic orbit.

D. Pairwise, distance-resolved, and subset-robust spatial coherence of the experimental DTQC state

The time-resolved measured-site coherence $|Z_{\Theta_+}^{(\mathcal{M})}(t)|$ used in the main text provides a compact summary of the measured-site phase memory of the locked sum phase. To resolve the spatial structure of that coherence more directly, we additionally evaluate pairwise and distance-resolved correlators on the same simultaneously recorded measured-site set $\mathcal{M} = \{7, 8, 9, 10\}$, and test the robustness of the resulting coherence against subset choice.

Using the reconstructed site-resolved sum phases $\Theta_{+,n}(t)$, we define the pairwise locked-phase coherence

$$C_{ij} \equiv \left| \left\langle e^{i[\Theta_{+,i}(t) - \Theta_{+,j}(t)]} \right\rangle_t \right|, \quad (\text{S104})$$

which quantifies the degree to which the locked DTQC phase remains aligned between measured sites i and j . We then define the distance-dependent coherence

$$C(r) \equiv \langle C_{ij} \rangle_{|i-j|=r}, \quad (\text{S105})$$

obtained by averaging over all measured-site pairs with separation r .

Figure S4.3(a) shows the resulting pairwise coherence matrix C_{ij} for the experimental DTQC operating point. The off-diagonal elements remain uniformly large across the measured-site set, indicating that the locked sum phase is not correlated only within a single channel pair. For comparison, we construct separate null references for the scalar instantaneous coherence and for the pairwise time-averaged coherence. For $|Z_{\Theta_+}^{(\mathcal{M})}(t)|$, the null reference is the finite-site random-phaser distribution with $N_{\mathcal{M}} = 4$, as described in Sec. S4B. For the pairwise quantity C_{ij} , the null reference is generated from independent random phase time series with the same number of samples and the same analysis window as the experimental trace. Equivalently, phase-shuffled surrogate traces may be used to preserve the single-site temporal statistics while destroying inter-site phase correlations. In this reference, the diagonal elements remain trivially unity, while the off-diagonal entries represent the 95th-percentile pairwise surrogate thresholds.

The corresponding distance-dependent coherence $C(r)$ is shown in Fig. S4.3(b). Over the accessible separations in the measured-site set, the experimental DTQC coherence remains well above the 95% random-phase reference. In this way, C_{ij} and $C(r)$ complement the scalar diagnostic $|Z_{\Theta_+}^{(\mathcal{M})}(t)|$: the latter provides a compact measured-site coherence measure, whereas the former show explicitly that the observed DTQC phase alignment is spatially shared across the simultaneously recorded measured sites rather than arising from averaging alone.

To test robustness with respect to subset choice, we further repeat the analysis for all three-site subsets of \mathcal{M} , which for the present four-site measured set is equivalent to a leave-one-out analysis. For each subset \mathcal{S} , we evaluate the time-averaged measured-site coherence

$$\bar{C}_{\Theta_+}^{(\mathcal{S})} \equiv \left\langle \left| Z_{\Theta_+}^{(\mathcal{S})}(t) \right| \right\rangle_t, \quad (\text{S106})$$

the mean off-diagonal pairwise coherence

$$\bar{C}_{ij}^{\text{offdiag},(\mathcal{S})} \equiv \left\langle C_{ij}^{(\mathcal{S})} \right\rangle_{i \neq j}, \quad (\text{S107})$$

and the fraction of times for which $|Z_{\Theta_+}^{(\mathcal{S})}(t)|$ exceeds the 95% finite-site random-phase baseline. As shown in Fig. S4.3(c), all three quantities remain uniformly large across the tested subsets. This confirms that the measured-site coherence reported in the main text is not dominated by a single measured site or by a particular three-site choice, but is robust across the simultaneously recorded measured-site set. For each three-site subset \mathcal{S} , the 95% finite-site random-phase baseline used for $|Z_{\Theta_+}^{(\mathcal{S})}(t)|$ is recomputed using $N_{\mathcal{S}} = 3$, rather than reusing the four-site baseline of the full measured set.

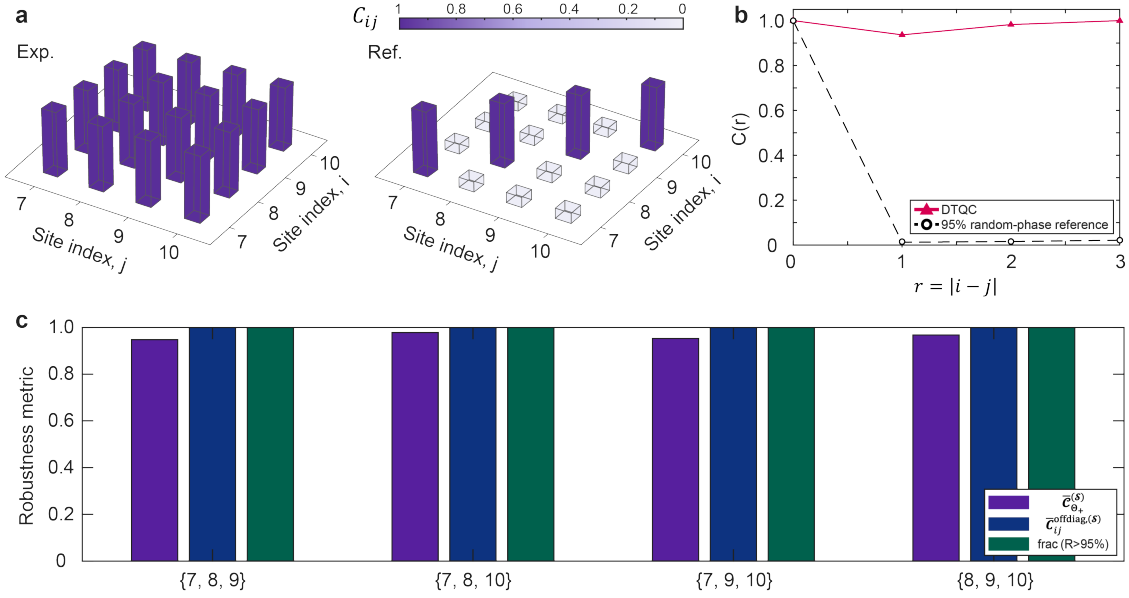


FIG. S4.3. **Pairwise, distance-resolved, and subset-robust spatial coherence of the experimental DTQC state.** (a) Pairwise locked-phase coherence matrix C_{ij} evaluated on the simultaneously recorded measured-site set $\mathcal{M} = \{7, 8, 9, 10\}$ (left), together with the corresponding 95% pairwise random-phase surrogate reference constructed using the same analysis window (right). The experimental DTQC state exhibits uniformly large off-diagonal coherence across the measured sites, whereas the surrogate reference retains only the trivial diagonal self-correlation and much smaller off-diagonal thresholds. (b) Distance-dependent coherence $C(r)$, obtained by averaging C_{ij} over all measured-site pairs with separation r . The measured DTQC coherence remains well above the corresponding 95% pairwise surrogate reference over the accessible separations. (c) Subset robustness of the measured-site coherence, evaluated over all three-site subsets of \mathcal{M} . Shown are the time-averaged measured-site coherence $\overline{C_{\Theta_+}^{(S)}} \equiv \langle |Z_{\Theta_+}^{(S)}(t)| \rangle_t$, the mean off-diagonal pairwise coherence $\overline{C_{ij}^{\text{offdiag}}}$, and the fraction of times for which $|Z_{\Theta_+}^{(S)}(t)|$ exceeds the 95% finite-site random-phase baseline recomputed for $N_S = 3$. All three metrics remain uniformly large across the tested subsets, showing that the observed coherence is not dominated by a single measured channel or by a particular subset choice.